Research Square

Preprints are preliminary reports that have not undergone peer review.
They should not be considered conclusive, used to inform clinical practice,
or referenced by the media as validated information.

The SCHENGEN pathway regulates lignin barrier formation via the receptor-like cytoplasmic kinase BIK1 in plant immunity

Ohkmae Park

omkim@korea.ac.kr

Korea University https://orcid.org/0000-0002-0234-6908

Eunjeong Jang
Korea University

Hwi Seong Jeon
Korea University

Minji Ahn
Korea University

Hyewon Cho
Korea University

Sewon Jeon
Korea University

May Thu Soe
Korea University

Yuki Tobimatsu
Kyoto University

Eunkyoo Oh
Korea University https://orcid.org/0000-0002-7313-2448

Article

Keywords:

Posted Date: March 16th, 2026

DOI: https://doi.org/10.21203/rs.3.rs-8962152/v1

License: This work is licensed under a Creative Commons Attribution 4.0 International License.
Read Full License

Additional Declarations: There is **NO** Competing Interest.

Version of Record: A version of this preprint was published at Nature Plants on October 29th, 2026. See the published version at https://doi.org/10.1038/s41477-026-02446-x.

The SCHENGEN pathway regulates lignin barrier formation via the receptor-like cytoplasmic kinase BIK1 in plant immunity

Eunjeong Jang[1,3], Hwi Seong Jeon[1,3], Minji Ahn[1], Hyewon Cho[1], Sewon Jeon[1], May Thu Soe[1], Yuki Tobimatsu[2], Eunkyoo Oh[1] & Ohkmae K. Park[1,*]

[1]Department of Life Sciences, Korea University, Seoul, Korea
[2]Research Institute for Sustainable Humanosphere, Kyoto University, Uji, Kyoto, Japan
[3]These authors contributed equally
[*]e-mail: omkim@korea.ac.kr

Corresponding Author:
Ohkmae K. Park
Department of Life Sciences
Korea University
Anam-dong, Seongbuk-gu
Seoul 02841, Korea
Phone: +82-2-3290-3458
E-mail: omkim@korea.ac.kr

Abstract

Lignin deposition is a hallmark of plant immunity, forming a physical barrier that restricts pathogen spread and confines hypersensitive cell death. However, how immune signaling triggers this barrier remains unclear. Here, we show that the Casparian strip surveillance pathway is repurposed during effector-triggered immunity to control lignin barrier formation. The peptide ligands CIF1 and CIF2 and their receptor SGN3 are transcriptionally induced upon avirulent bacterial infection and are required for pathogen-induced lignification and disease resistance. Mechanistically, SGN3 directly interacts with and phosphorylates BIK1, which acts as the primary downstream receptor-like cytoplasmic kinase in immune signaling. Genetic and molecular analyses further reveal that NLR-driven CIFs-SGN3-BIK1 signaling cooperates with pattern-recognition receptor pathways to promote ROS production and lignin polymerization during ETI. These findings uncover a previously unrecognized immune function of the SGN pathway and establish a signaling module linking pathogen recognition to lignin-based barrier formation.

Introduction

As sessile organisms, plants have evolved the sophisticated immune systems to protect themselves from a wide range of pathogens. The first layer of defense, pattern-triggered immunity (PTI), is initiated when cell-surface pattern recognition receptors (PRRs) perceive pathogen-associated molecular patterns (PAMPs) or damage-associated molecular patterns (DAMPs) (Boller and Felix, 2009; Zipfel, 2014; Bartels and Boller, 2015; Choi and Klessig, 2016; Couto and Zipfel, 2016; Hou et al., 2019; Cho et al., 2023). Among the best-characterized PRRs are the leucine-rich repeat receptor kinases (LRR-RKs), such as FLAGELLIN SENSING 2 (FLS2), EF-TU RECEPTOR (EFR), and PLANT ELICITOR PEPTIDE RECEPTOR 1 and 2 (PEPR1/2) (Zipfel et al., 2006; Chinchilla et al., 2007; Yamaguchi et al., 2010). Upon ligand binding, these receptors form active complexes with the co-receptors BRASSINOSTEROID INSENSITIVE 1 (BRI1)-ASSOCIATED RECEPTOR KINASE 1 (BAK1)/SOMATIC EMBRYOGENESIS RECEPTOR KINASE 3 (SERK3) and related SERK family members (Chinchilla et al., 2007; Sun et al., 2013). The activated receptor complexes then phosphorylate receptor-like cytoplasmic kinases (RLCKs), notably BOTRYTIS-INDUCED KINASE 1 (BIK1) and its close homologs, the AVRPPHB SUSCEPTIBLE 1 (PBS1)-LIKE (PBL) proteins, triggering downstream immune signaling (Lu et al., 2010; Li et al., 2014; Bi et al., 2018; Jiang et al., 2019). However, adapted pathogens can suppress PTI by delivering effectors into host cells, enabling disease development. To counter this, plants employ intracellular nucleotide-binding LRR containing receptors (NLRs) that detect these effectors and activate effector-triggered immunity (ETI), a second defense layer associated with a localized hypersensitive response (HR), a form of programmed cell death (PCD) (Li et al., 2015; Huh et al., 2017; Wang et al., 2019). Recent evidence reveals that PTI and ETI are intricately interconnected: ETI potentiates PTI, and PTI components are essential for ETI activation (Ngou et al., 2021; Pruitt

et al., 2021; Tian et al., 2021; Yuan et al., 2021a). Together, PTI and ETI orchestrate overlapping immune responses, including reactive oxygen species (ROS) burst, Ca^{2+} influx, mitogen-activated protein kinase (MPK) activation, and cell wall reinforcement such as lignin deposition (Chezem et al., 2017; Yuan et al., 2021b; Chang et al., 2022).

Lignin, a complex phenolic polymer, is primarily composed of three monolignols—*p*-coumaryl, coniferyl, and sinapyl alcohols—which are oxidatively polymerized into *p*-hydroxyphenyl (H), guaiacyl (G), and syringyl (S) lignin units, respectively (Vanholme et al., 2019; Yao et al., 2021; Zhang et al., 2021). Monolignols are synthesized in the cytosol via the phenylpropanoid pathway and subsequently exported to the apoplast, where they are polymerized into lignin by oxidative enzymes such as laccases and peroxidases (Alejandro et al., 2012; Sibout and Höfte, 2012; Jeon et al., 2023). This process requires ROS generated by NADPH oxidases, also known as respiratory burst oxidase homologs (RBOHs) (Lee et al., 2013; Tobimatsu and Schuetz, 2019; Rojas-Murcia et al., 2020). Lignin is an essential structural component of the secondary cell wall, forming the lignified xylem vessels and fibers (Barros et al., 2015; Liu et al., 2018). The role of lignin as a diffusion barrier has been exemplified by the Casparian strip, which is constructed by localized lignin deposition in the primary cell wall and seals the extracellular space between root endodermal cells (Roppolo et al., 2011; Naseer et al., 2012; Lee et al., 2013). Casparian strip formation requires Casparian strip membrane domain proteins (CASPs) and dirigent proteins (DIRs) to ensure spatially precise lignification (Roppolo et al., 2011; Gao et al., 2023). Genetic and molecular studies have identified the SCHENGEN (SGN) signaling pathway as a surveillance system for Casparian strip integrity. This pathway includes the peptide ligands CASPARIAN STRIP INTEGRITY FACTOR 1 and 2 (CIF1/2), their cognate receptor SGN3, also known as GASSHO 1 (GSO1), and the downstream RLCK SGN1 (Pfister et al., 2014; Doblas et al., 2017; Nakayama et al., 2017; Okuda et al., 2020). SGN1 phosphorylates RBOHD and RBOHF, driving ROS production and

localized lignin polymerization at the Casparian strip (Alassimone et al., 2016; Doblas et al., 2017; Fujita et al., 2020)

Beyond its roles in development, lignin is recognized as a critical component of the plant immune system, functioning as a physical barrier against pathogen invasion (Malinovsky et al., 2014; Cesarino, 2019; Ma, 2024; Molina et al., 2024). PTI-associated lignification is rapidly induced in *Arabidopsis* seedlings and roots upon treatments with PAMP or DAMP elicitors such as flg22, elf18, and Pep1, and is largely under transcriptional control (Adams-Phillips et al., 2009; Chezem et al., 2017; Zhang et al., 2022b). The SG2-type R2R3-MYB transcription factor MYB15 activates lignin biosynthetic genes, including *PHENYLALANINE AMMONIA LYASE* (*PAL*) and *CINNAMATE 4-HYDROXYLASE* (*C4H*) (Kim et al., 2020). Pep1-induced lignification is abolished in *bak1 serk4*, *bik1 pbl1*, and *rbohD/F* mutants, underscoring the essential role of PTI signaling components in lignin accumulation (Zhang et al., 2022b). Our recent findings demonstrate that lignin deposition is strongly induced during ETI, which not only restricts pathogen spread but also confines HR-associated cell death (Lee et al., 2019; Kim et al., 2020; Jeon et al., 2023). This process requires CASP-like (CASPL) proteins, CASPL1D1 and CASPL4D1, implying that lignin, together with CASPLs, establishes a mechanical barrier analogous to the endodermal Casparian strip. Moreover, lignin biosynthetic gene expression and disease resistance are compromised in *myb15* mutant plants challenged with avirulent bacterial pathogens, indicating that MYB15 is indispensable for pathogen-induced lignin biosynthesis (Kim et al., 2020).

Here, we report that the Casparian strip-associated SGN pathway plays a key role in establishing a lignin-based barrier during ETI. We show that SGN3 and its peptide ligands CIF1/2 are transcriptionally activated upon avirulent bacterial infection, and that their mutants display defective lignification, allowing pathogens and HR cell death to spread beyond the infection site. Notably, SGN3 interacts with and phosphorylates BIK1, establishing a novel

signaling module that links receptor activation to lignin biosynthesis. Our findings reveal a previously unrecognized immune function of the SGN pathway and extend its developmental role to the regulation of pathogen-induced lignification.

Results

SGN3/GSO1 is required for lignin barrier formation in ETI

In our previous study, we demonstrated that a physical barrier is rapidly established at the infection site challenged with avirulent pathogens, effectively restricting the spread of pathogens and HR PCD and thereby contributing to disease resistance (Lee et al., 2019). Because this barrier formation occurs immediately after pathogen infection, we sought to identify the upstream signaling pathway that triggers its induction. Lignin serves as a major structural component of this immune-associated barrier and CASPL proteins are required for its formation, which are structural features shared with the Casparian strip in the root endodermis. This similarity led us to investigate whether the SGN signaling pathway—known to govern Casparian strip formation—also plays a role in the induction of the lignin-based barrier during immune responses.

To explore this, we examined the possible involvement of a key SGN component SGN3/GSO1 and its homolog GSO2. In addition, we included PEPR1/2 in our study, as these receptors are closely related to SGN3/GSO1 and GSO2 in phylogenetic analysis and have been implicated in plant defense and lignin deposition (Yamaguchi et al., 2010; Engelsdorf et al., 2018) (Extended Data Fig. 1). We first analyzed the expression of these genes following inoculation with different *Pseudomonas syringae* pv. *tomato* (*Pst*) DC3000 strains, including the PTI-inducing *Pst* DC3000 *hrcC*$^{-}$, virulent *Pst* DC3000, and avirulent *Pst* DC3000 (*AvrRpm1*). Their transcript levels were normally very low but strongly elevated upon infection

with *Pst* DC3000 (*AvrRpm1*) (Fig. 1a), suggesting that these receptors are transcriptionally activated during ETI. To determine whether these receptors contribute functionally to lignin barrier formation, we inoculated the T-DNA insertion single mutants *sgn3-4*, *gso1-2*, *gso2-1*, and *gso2-2* (Racolta et al., 2014) and double mutants *pepr1-1 pepr2-1* and *pepr1-2 pepr2-2* (Yamaguchi et al., 2010) with *Pst* DC3000 (*AvrRpm1*) and assessed lignification at the infection site by phloroglucinol staining and acetyl bromide-based quantification. Lignin accumulation was not affected in *gso2* and *pepr1 pepr2* plants but was defective in *sgn3-4* and *gso1-2* plants (Fig. 1b,c). Consistently, HR cell death spread over the infection site in *sgn3-4* and *gso1-2* leaves (Fig. 1d,e). These results suggest that SGN3/GSO1 is a key regulator of lignin barrier formation in ETI.

CIF1 and CIF2 function as primary ligands for SGN3 during ETI

To test whether the SGN3 ligands CIF1 and CIF2 are also involved, we analyzed *AvrRpm1*-induced lignification in *cif1-1* (Nakayama et al., 2017) and *cif2-1* (Wang et al., 2021) single mutants and the *cif1 cif2* double mutant generated by CRISPR-Cas9 (Fujita et al., 2020). Each single mutant showed no obvious defects; however, *cif1 cif2* plants were impaired in lignification and localized HR cell death (Fig. 2a-c), consistent with their known functional redundancy. We next examined whether exogenous peptide application could compensate for the loss of endogenous CIFs. Co-inoculation of *cif1 cif2* leaves with *Pst* DC3000 (*AvrRpm1*) and synthetic CIF1 peptide restored lignin accumulation to wild-type levels (Fig. 2d,e) and limited the spread of HR cell death (Fig. 2f,g). Consistent with these defects, *cif1 cif2* plants exhibited reduced disease resistance (Fig. 2h) and the pathogen spread into the surrounding uninfected area, as visualized using GFP-labeled Pst DC3000 (*AvrRpt2*) (Fig. 2i). CIF1 peptide treatment rescued these immune defects in *cif1 cif2* plants but had no measurable effect in *sgn3-4* mutant (Fig. 2d-i), as expected given that SGN3 acts as the receptor for CIF1/2. These results

demonstrate that, analogous to their function in Casparian strip formation, CIF1/2 peptides and their receptor SGN3 constitute a core signaling module required for lignin barrier formation in ETI.

Structure-guided sequence analysis revealed CIF3 and CIF4 as additional CIF family members, and *in vitro* binding assays showed that all four peptides (CIF1 to CIF4) bind to SGN3 with high affinity (Okuda et al., 2020). We therefore investigated whether these CIF peptides participate in immune-induced lignification. Following pathogen challenge, the transcript levels of *CIF1* to *CIF4*—normally very low—were strongly increased by *Pst* DC3000 (*AvrRpm1*) infection (Extended Data Fig. 2a). Likewise, similar to CIF1 (Fig. 2d,e), exogenous application of other CIF peptides also restored lignin deposition in the *cif1 cif2* mutant (Extended Data Fig. 2b). However, in contrast to defects observed in *cif1 cif2* and *cif1 cif2 cif3 cif4* (Doll et al., 2020) mutants, the *cif3 cif4* mutant (Okuda et al., 2020) showed wild-type levels of lignification and HR restriction (Extended Data Fig. 2c-f). These findings suggest that although all four CIF peptides can engage SGN3, CIF1 and CIF2 serve as the primary functional ligands for SGN3 during immune-associated lignin barrier formation.

SGN3 kinase controls lignin barrier formation during ETI

To further validate the role of SGN3, we generated complementation lines expressing either wild-type SGN3 ($SGN3^{WT}$-eGFP) or a kinase-dead variant ($SGN3^{K979E}$-eGFP) in the *sgn3-4* mutant (Extended Data Fig. 3a,b). Expression of $SGN3^{WT}$-eGFP, but not $SGN3^{K979E}$-eGFP, fully restored lignin accumulation (Extended Data Fig. 3c; Fig. 3a,b), localized cell death (Extended Data Fig. 3d; Fig. 3c,d), and disease resistance (Fig. 3e) in *sgn3-4* plants. These results further demonstrate that SGN3 is essential for ETI-associated lignification and disease resistance and that its kinase activity is required for these functions. Notably, CIF1 treatment alone induced lignin accumulation in $SGN3^{WT}$-eGFP *sgn3-4* plants (Fig. 3f), suggesting that

CIF-mediated SGN3 activation is sufficient to drive lignin barrier formation.

Next, we examined the subcellular localization of SGN3 and lignin in $SGN3^{WT}$-eGFP *sgn3-4* plants. As previously reported (Lee et al., 2019), lignin deposition can be visualized using fluorescence-tagged monolignols, such as dimethylaminocoumarin-coniferyl alcohol (CADMAC) (Tobimatsu et al., 2013). Using this approach, plants were supplied with CADMAC during *Pst* DC3000 (*AvrRpm1*) infection. Under these conditions, SGN3-eGFP localized to the plasma membrane, whereas lignin accumulated in the extracellular region proximal to SGN3 (Fig. 3g,h).

BIK1 functions downstream of the CIF1/2–SGN3 complex to promote ETI-associated lignification

We sought to identify the RLCK that transmits signals downstream of the CIF1/2-SGN3 receptor complex. Given that BIK1 and SGN1 function as key RLCKs in immune signaling (Lu et al., 2010; Liu et al., 2013; Li et al., 2014) and Casparian strip development (Fujita et al., 2020), respectively, we investigated their potential involvement in this pathway. We first examined the transcriptional responses of *BIK1* and *SGN1* following pathogen inoculation. As previously reported (Ngou et al., 2021; Yuan et al., 2021a), *BIK1* expression was induced under PTI conditions triggered by *Pst* DC3000 *hrcC*$^{-}$ and was even more strongly upregulated upon ETI activation by *Pst* DC3000 (*AvrRpm1*) (Fig. 4a). In contrast, *SGN1* transcript levels increased only modestly at 16 h after *Pst* DC3000 (*AvrRpm1*) infection and remained substantially lower than those of *BIK1*. Consistent with these expression patterns, the *bik1* mutant (Lu et al., 2010) displayed pronounced defects in ETI-associated lignin deposition (Fig. 4b,c), restriction of HR PCD (Fig. 4d,e), and disease resistance (Fig. 4f). By contrast, the *sgn1-2* mutant (Alassimone et al., 2016) showed responses indistinguishable from Col-0 across these phenotypes, suggesting that BIK1, but not SGN1, is required for immune-induced lignification.

Because RLCK phosphorylation is a hallmark of PRR signaling (Lu et al., 2010; Liu et al., 2013; Li et al., 2014; Fujita et al., 2020), we next tested whether CIF peptide perception by SGN3 leads to phosphorylation of BIK1 or SGN1. Because BIK1 phosphorylation is commonly detected as a mobility shift in immunoblot analysis following flg22 treatment (Lee et al., 2017), we used this assay to assess phosphorylation of BIK1 and SGN1 in mesophyll protoplasts. BIK1 or SGN1 was expressed either alone or together with SGN3, followed by treatment with flg22 or CIF peptides. As expected, slower-migrating BIK1 was observed upon flg22 treatment (Fig. 4g). CIF peptide-induced BIK1 mobility shifts were significantly induced only when SGN3 was co-expressed, consistent with low endogenous expression of SGN3 in Col-0 leaves. In contrast, SGN1 exhibited no detectable band shift. Previous studies have shown that the kinase-dead mutant BIK1^{K105E} fails to exhibit the flg22-induced mobility shift, indicating that BIK1 phosphorylation requires its intrinsic kinase activity and the band shift is largely due to BIK1 autophosphorylation (Li et al., 2014). In line with this observation, BIK1^{K105E} expression abolished the flg22- and CIF2-induced electromobility retardation of BIK1 (Extended Data Fig. 4a). Moreover, application of the CIF2^{I81D} peptide (Okuda et al., 2020), which acts as a dominant-negative ligand by disrupting the SGN3-SERK interaction, was unable to elicit a BIK1 mobility shift. When tested in *fls2* and *sgn3-4* backgrounds, flg22-induced BIK1 phosphorylation occurred independently of SGN3 expression but was completely abolished in *fls2* mutant. However, the CIF1-induced BIK1 mobility shift was observed in Col-0, *fls2*, and *sgn3-4* protoplasts, provided that SGN3 was ectopically expressed (Extended Data Fig. 4b). Consistently, the CIF1-induced BIK1 band shift was detected in SGN3^{WT}-eGFP *sgn3-4* plants, but not in SGN3^{K979E}-eGFP *sgn3-4*, and was reversed upon calf alkaline intestinal phosphatase treatment (Extended Data Fig. 4c).

To validate these results, we employed a rapamycin-inducible dimerization (RiD) receptor system (Kim et al., 2021). In this system, the cytoplasmic kinase domain (KD) of two

receptors are fused to FK506-binding protein 12 (FKBP) and FKBP-rapamycin-binding (FRB) domains, respectively, and are targeted to the plasma membrane by an N-terminal myristoylation signal (Fig. 4h). Upon rapamycin treatment, FKBP-FRB dimerization induces receptor interaction and downstream signaling. Using this system, we transiently expressed either FLS2 KD-FKBP or SGN3 KD-FKBP, together with the co-receptor BAK1 KD-FRB, while simultaneously expressing either BIK1 or SGN1. Rapamycin-induced dimerization of both FLS2-BAK1 and SGN3-BAK1 resulted in robust mobility shifts of BIK1, whereas no slower-migrating form of SGN1 was detected (Fig. 4i). Notably, mobility shifts of SGN3 and BAK1 themselves were also observed in the SGN3-BAK1 complex. Although SGN1 is phosphorylated by SGN3 *in vitro* (Fujita et al., 2020), the absence of a detectable shift here suggests that alternative assays may be required to assess SGN1 phosphorylation. Together, these findings demonstrate that BIK1—but not SGN1—acts as the primary RLCK downstream of the CIF1/2-SGN3 receptor complex, establishing a direct mechanistic link between CIFs-SGN3 signaling and immune-associated lignin barrier formation.

To further assess whether SGN3 functionally depends on BIK1, we crossed SGN3^{WT}-eGFP *sgn3-4* plants with the *bik1* mutant and examined immune responses in the resulting crossed lines. Pathogen-induced lignification observed in SGN3^{WT}-eGFP *sgn3-4* plants, together with restricted HR cell death and disease resistance, was all impaired, showing phenotypes comparable to those of the *bik1* mutant (Fig. 4j-n). Moreover, CIF1-induced lignin deposition was abolished in these crossed lines, as in the *bik1* mutant (Fig. 4o). These results underscore that BIK1 is indispensable for SGN3-mediated immune responses, further establishing BIK1 as an essential downstream component of SGN3 signaling.

SGN3 physically interacts with and phosphorylates BIK1

Given the downstream role of BIK1 in SGN3 signaling, we examined whether SGN3

physically interacts with BIK1. An *in vitro* pull-down assay revealed a direct interaction between BIK1 and SGN3 KD (Fig. 5a). To test this interaction *in vivo*, we conducted a bimolecular fluorescence complementation (BiFC) assay in protoplasts by co-expressing SGN3 and BIK1 fused to the N- and C-terminal fragments of YFP. Reconstituted YFP fluorescence indicated that SGN3 and BIK1 interact at the plasma membrane (Fig. 5b). Consistently, co-immunoprecipitation analysis further verified their *in vivo* association (Fig. 5c).

Because PRRs have been shown to promote BIK1 phosphorylation (Lu et al., 2010; Cao et al., 2013; Liu et al., 2013; Lal et al., 2018), we asked whether SGN3 is similarly capable of phosphorylating BIK1. To address this, we performed *in vitro* kinase assays using SGN3 KD and BIK1 recombinant proteins. To specifically assess transphosphorylation and eliminate contributions from autophosphorylation, the kinase-dead mutant $BIK1^{K105E}$ was used as a substrate (Fig. 5d). SGN3 KD^{WT}, but not the kinase-dead mutant SGN3 KD^{K979E}, displayed autophosphorylation activity and efficiently transphosphorylated $BIK1^{K105E}$.

To further define the SGN3-dependent phosphorylation of BIK1, we next examined whether residues previously reported to be phosphorylated by PRRs, BAK1, and BIK1 itself are also targeted by SGN3. We generated a series of $BIK1^{K105E}$ mutants in which known phosphosites were additionally substituted with Ala (for Ser/Thr) or Phe (for Tyr) and tested their phosphorylation by SGN3 KD *in vitro*. The mutated residues included S89 and T90, phosphorylated by EFR (Lal et al., 2018); S236, phosphorylated by PEPR1 (Liu et al., 2013); T237, a shared target site by FLS2, PEPR1, and BAK1 and also subject to BIK1 autophosphorylation (Lu et al., 2010; Liu et al., 2013; Lin et al., 2014); Y243 and Y250, phosphorylated by BAK1 and BIK1 itself (Lin et al., 2014); and Y150 and T242, identified as BIK1 autophosphorylation sites (Lin et al., 2014).

In vitro kinase assays revealed that phosphorylation of most BIK1 mutants was reduced

compared with BIK1^{K105E}, with the T237A substitution showing the most pronounced effect, reducing phosphorylation by more than 80% (Fig. 5e). To assess the *in vivo* relevance of these residues, we performed transient expression assays in protoplasts and monitored CIF1-induced BIK1 mobility shifts as an indicator of BIK1 autophosphorylation. Whereas the S89A/T90A and Y243F mutants exhibited mobility shifts comparable to wild-type BIK1, a moderate reduction was observed in Y150F, S236A, T242A, and Y250F mutants. Notably, the BIK1^{T237A} mutant displayed a dramatic loss of mobility shift, comparable to that observed for the kinase-dead BIK1^{K105E} mutant (Fig. 5f). S89A/T90A and Y243F mutants exhibited differential phosphorylation patterns between two assays, raising the possibility that these residues are phosphorylated by SGN3 but do not critically contribute to BIK1 kinase activation. Together, these results demonstrate that SGN3 directly and specifically phosphorylates BIK1 and that T237 is a key residue required for SGN3-mediated BIK1 activation in immune signaling.

NLR-driven SGN3–BIK1 signaling cooperates with PRR signaling to regulate lignin barrier formation during ETI

Because lignification contributes to both PTI and ETI (Chezem et al., 2017; Lee et al., 2019), we examined whether PTI-associated lignin deposition is driven solely by canonical PRR signaling or also requires the SGN3-BIK1 module. Upon treatment with flg22 or Pep1, *MYB15* expression was induced together with the PTI marker gene *FLG22-INDUCED RECEPTOR-LIKE KINASE 1* (*FRK1*) in Col-0, but not in *fls2* or *pepr1-1 pepr2-1* plants, whereas *SGN3* and *CIF1* showed no significant transcriptional induction (Extended Data Fig. 5a,b). Similarly, flg22 and Pep1 treatments induced lignin deposition in Col-0 plants, whereas this increase was not observed in the corresponding *fls2* and *pepr1-1 pepr2-1* mutants (Extended Data Fig. 5c,d). In addition, inoculation with *Pst* DC3000 *hrcC*$^{-}$ also enhanced lignin accumulation, but this response was abolished in the *fls2* mutant (Extended Data Fig. 5e,f). These results demonstrate

312 that PTI-associated lignification is mediated through PRR signaling.

313 Next, we investigated whether PTI components are involved in lignin formation during
314 ETI. Notably, *Pst* DC3000 (*AvrRpm1*)-induced lignification occurred at near Col-0 levels in
315 *fls2* and *pepr1-1 pepr2-1* mutants (Extended Data Fig. 5e,f). However, as the use of individual
316 PRR mutants is insufficient to assess the contribution of PTI signaling, we conducted additional
317 experiments to clarify PTI involvement. Previous studies demonstrate that PTI and ETI are
318 interconnected and mutually required for full immune activation (Ngou et al., 2021; Yuan et
319 al., 2021a). To address whether PRR signaling contributes to ETI-associated lignification, we
320 employed previously characterized PRR/co-receptor mutants with compromised PTI signaling,
321 *fls2 efr cerk1* (*fec*) and *bak1 bkk1 cerk1* (*bbc*) (Yuan et al., 2021a). Given that SGN3 requires
322 SERK co-receptors for signaling (Okuda et al., 2020; Zhang et al., 2022a), we anticipated that
323 the *fec* mutant would impair PTI-associated lignification, whereas the *bbc* mutant would affect
324 lignification associated with both PTI and ETI.

325 We first examined the expression of genes comprising the SGN3-BIK1 module
326 following inoculation with *Pst* DC3000 (*AvrRpm1*). Transcript levels of *SGN3*, *CIF1*, and *BIK1*
327 in *fec* and *bbc* mutants were comparable to those in Col-0 (Fig. 6a). In contrast, induction of
328 these genes was markedly reduced in the *rpm1-3 rps2-101c* mutant, which is defective in NLR-
329 mediated recognition of AvrRpm1 (Fig. 6b). Conversely, in transgenic plants expressing
330 dexamethasone (Dex)-inducible AvrRpm1, Dex treatment strongly induced expression of
331 *SGN3*, *CIF1*, and *BIK1* (Fig. 6c). Together, these results suggest that transcriptional activation
332 of the SGN3-BIK1 module during ETI is specifically driven by NLR signaling rather than
333 PRR-mediated pathways.

334 With respect to lignin deposition, PTI-induced lignification triggered by flg22, Pep1, or
335 *Pst* DC3000 *hrcC*$^{-}$ was impaired in *fec* and *bbc*, but not in *sgn3-4* plants, suggesting that SGN3
336 signaling is not required for PTI-associated lignin deposition (Fig. 6d-f). In contrast,

337 lignification triggered by *Pst* DC3000 (*AvrRpm1*) was severely impaired in *sgn3-4*, *bik1*, and
338 *bbc* mutants and was markedly reduced in the *fec* mutant (Fig. 6e,f), implying that PRR
339 signaling contributes substantially to lignification during ETI. Meanwhile, *Pst* DC3000
340 (*AvrRpm1*)-induced expression of the lignin biosynthetic genes *PAL1* and *C4H* as well as their
341 key regulator *MYB15* showed partial but significant decrease in *sgn3-4*, *cif1 cif2*, *fec*, and *bbc*
342 mutants, and was even more strongly reduced in *bik1* plants (Extended Data Fig. 6a,b). These
343 results suggest that both NLR and PRR signaling pathways transcriptionally regulate
344 monolignol biosynthesis, largely through BIK1.

345 Previous studies have shown that BIK1-mediated activation of RBOHD and the resulting
346 ROS burst serve as a key node linking PTI and ETI (Ngou et al., 2021; Yuan et al., 2021a). We
347 therefore monitored ROS production in response to *Pst* DC3000 (*AvrRpm1*) using the
348 fluorescent dye H_2DCFDA. ROS accumulation was reduced in the *fec* mutant and was severely
349 compromised in *bbc*, *sgn3-4*, and *bik1* mutants (Fig. 6g,h). However, *RbohD* expression was
350 only modestly decreased in *bik1* and unaffected in *sgn3-4* plants (Fig. 6i). These results
351 demonstrate that PRR signaling contributes to ROS burst during ETI and further suggest that
352 the SGN3-BIK1 module plays a critical role in promoting ROS production, thereby driving
353 immune-associated lignin barrier formation (Fig. 6j).

354

355 **Discussion**

356

357 In this study, we identify the SGN surveillance pathway as a central regulator of immune-
358 associated lignin barrier formation during ETI. We demonstrate that the peptide ligands CIF1
359 and CIF2 and their receptor SGN3 (also known as GSO1), previously characterized for their
360 developmental roles in Casparian strip formation, are transcriptionally induced upon avirulent
361 pathogen infection and are essential for pathogen-induced lignification, restricting pathogen

spread and confining hypersensitive cell death. Our findings reveal that plants repurpose a surveillance mechanism for Casparian strip integrity to rapidly establish a lignin-based physical barrier during immune responses.

Previous studies have demonstrated that the CIFs-SGN3 signaling module plays a central role in Casparian strip formation in roots, where CIF1 and CIF2 peptides are synthesized in the stele and diffuse toward the endodermis to activate SGN3, thereby inducing localized lignification and diffusion barrier formation (Pfister et al., 2014; Doblas et al., 2017; Nakayama et al., 2017). In contrast, the SGN3 homolog GSO2 and the related peptides CIF3 and CIF4 are not detectably expressed in roots, and their loss does not affect Casparian strip formation (Tsuwamoto et al., 2008; Okuda et al., 2020), suggesting that the apparent dispensability of these components in Casparian strip formation may simply reflect the absence of their expression in root tissues. Notably, SGN3/GSO1 and GSO2 function redundantly in the formation of other barrier structures, such as the embryonic cuticle and pollen wall, where distinct CIF family peptides—TWISTED SEED 1 (TWS1) and CIF3/CIF4, respectively—act as their functional ligands (Doll et al., 2020; Truskina et al., 2022; Zhang et al., 2022a). Together, these studies position SGN3 and GSO receptors as broadly conserved barrier surveillance kinases with context-dependent biological outputs.

In our study, we demonstrate that SGN3 and CIF1/2 are redeployed in immune responses to drive lignin-based barrier formation. Interestingly, although GSO2 and CIF3/4 do not function in ETI-associated lignification, their transcripts were strongly induced following avirulent pathogen challenge. While protein-level expression is yet to be determined, this transcriptional activation raises the possibility that these components participate in other immune-related processes that remain to be uncovered. An additional layer of regulation may lie at the level of peptide maturation. CIF1 and CIF2 are C-terminally encoded peptides that do not require proteolytic C-terminal processing, whereas CIF3, CIF4, and TWS1 depend on

subtilase-mediated C-terminal cleavage for activation (Doll et al., 2020; Truskina et al., 2022). It is therefore conceivable that, during ETI, the absence or limited activity of the relevant processing proteases prevents CIF3/CIF4 activation, rendering them functionally inert despite transcriptional induction. This highlights post-translational peptide processing as a potential regulatory step that determines ligand specificity.

A key question raised by our findings is why plants require an SGN3-dependent pathway for lignification during ETI when PRR signaling can already induce lignification during PTI. Major PTI components, including FLS2, EFR, BAK1, and BIK1, are widely recognized targets of pathogen effectors (Göhre et al., 2008; Shan et al., 2008; Xiang et al., 2008; Zhang et al., 2010). Consequently, effective reliance on canonical PRR signaling during ETI would require quantitative and qualitative restoration of PTI components that have been suppressed or deformed by effectors. Indeed, recent studies have shown that ETI depends on PTI, and that this dependency is fulfilled primarily through a quantitative increase in selected PTI signaling components (Ngou et al., 2021; Yuan et al., 2021a). Notably, ETI is accompanied by marked accumulation of BIK1, BAK1, and RBOHD, whereas other components such as FLS2, CERK1, and MPK4/6 do not increase as clearly (Ngou et al., 2021). These observations suggest that the BIK1-RBOHD-ROS burst constitutes a central axis of ETI, and that enhanced abundance and activation of BIK1 and RBOHD may allow plants to partially overcome effector-mediated suppression of PTI signaling. Within this framework, the deployment of SGN3 during ETI becomes conceptually compelling. CIF1/2 and SGN3 are barely expressed in leaf tissues under basal or PTI conditions, but are rapidly and strongly induced specifically during ETI via NLR signaling, allowing the *de novo* assembly of a fresh receptor module. We therefore speculate that plants have evolved to deploy SGN3 as an alternative or bypass signaling module that converges on the BIK1-RBOHD axis, thereby ensuring robust lignin deposition even when effector-targeted PRR modules are functionally compromised.

A central insight from this work is that SGN3 engages distinct downstream RLCKs depending on developmental or immune contexts. In the root endodermis, SGN1 functions as the primary RLCK downstream of SGN3 to regulate Casparian strip formation. By contrast, during ETI in leaves, SGN3 switches its signaling partner to the immune-associated BIK1. SGN3 physically interacts with and phosphorylates BIK1, and loss of BIK1 abolishes SGN3-driven lignification and immune responses. Why might plants favor BIK1 over SGN1 in immunity? One explanation lies in signaling specificity conferred by MPK cascades. MPK signaling pathways transmit signals from cell surface receptors to the nucleus through MPK kinase kinase (MPKKK), MPK kinase (MPKK), and MPK (Andreasson and Ellis, 2010; Ma and Nicolet, 2023). Importantly, distinct MPK cascades give rise to divergent developmental or immune outputs. A recent study in the root endodermis demonstrates that the SGN3 and FLS2 pathways engage different MKKs and MPKs, resulting in distinct transcriptional and cellular responses (Ma et al., 2024). RLCKs serve as critical nodes linking receptor kinases to these MPK cascades, thereby shaping signaling specificity (Cui et al., 2018). Given that SGN1 expression is largely restricted to the endodermis and is not strongly induced during ETI, whereas BIK1 is widely expressed and rapidly upregulated upon pathogen challenge, it is plausible that SGN3 signaling is rewired toward an immune-adapted BIK1-MPK axis during ETI. Such selective recruitment of BIK1 may ensure robust lignin-based barrier formation and other immune responses, while preserving developmental specificity of the SGN1-dependent pathway in roots.

BIK1 is well established as a central signaling hub that associates with multiple PRRs, including FLS2, EFR, and PEPR1, as well as the co-receptor BAK1, to transduce immune signals during PTI. Our study extends this repertoire by identifying SGN3 as an additional LRR-RK that interacts with BIK1 and is uniquely associated with ETI. Previous studies have identified multiple residues in BIK1 that are phosphorylated by PRRs, BAK1, and BIK1 itself.

For example, EFR-mediated phosphorylation occurs at S89 and T90 (Lal et al., 2018), PEPR1 phosphorylates S236 and T237 (Liu et al., 2013), and BAK1 targets T237, Y243, and Y250 (Lin et al., 2014). T237 phosphorylation is also induced by flg22 treatment and is therefore considered a key residue for FLS2-mediated BIK1 activation (Lu et al., 2010). In addition, several residues, including Y150, T237, T242, Y243, and Y250, have been identified as autophosphorylation sites of BIK1 (Liu et al., 2013; Lin et al., 2014). Interestingly, substitution of these residues with Ala or Phe in *in vitro* kinase assays consistently reduced SGN3-mediated BIK1 phosphorylation, albeit to varying extents, with the T237A mutation having the most pronounced effect. These results indicate that SGN3 is capable of phosphorylating multiple Ser/Thr and Tyr residues on BIK1, many of which overlap with sites previously implicated in PRR signaling. Whether these residues function as bona fide SGN3-dependent phosphosites *in vivo* and how such phosphorylation events impact immune responses remain important questions for future studies.

Meanwhile, analysis of BIK1 mobility shifts, which mainly reflect BIK1 autophosphorylation, further revealed that the S89A/T90A and Y243F substitutions—both of which reduced SGN3-dependent BIK1 phosphorylation *in vitro*—had little effect on BIK1 mobility shifts, but the T237A mutation largely abolished the shifted band of BIK1. These results identify T237 as a key residue both for SGN3-mediated phosphorylation and for BIK1 autophosphorylation. Notably, this is consistent with previous studies showing that T237 represents a major phosphorylation site commonly targeted by multiple PRRs and BAK1 as well as by BIK1 itself (Lu et al., 2010; Liu et al., 2013; Lin et al., 2014). Elucidating the functional consequences of BIK1 phosphorylation—such as its role in activating BIK1 kinase, generating docking sites for its interacting partners, and specifying immune outputs—together with the identification of BIK1 downstream signaling components in the SGN pathway, will be critical for defining the molecular framework through which SGN signaling contributes to

plant immunity.

In conclusion, our study suggests that plants have evolutionarily repurposed a developmental barrier surveillance pathway to reinforce immunity. The CIF-SGN3 module, long regarded as a regulator of Casparian strip integrity in roots, is largely inactive in leaf tissues under normal conditions but is rapidly transcriptionally activated upon pathogen invasion. This functional redeployment highlights the remarkable plasticity of receptor signaling networks in plants. By switching its downstream signaling partner from SGN1 to BIK1, SGN3 is incorporated into canonical immune signaling circuitry while preserving its core role in barrier formation. Our findings support a model in which SGN3 serves as an alternative immune receptor, complementing conventional PRRs during ETI. This ensures effective defense even when canonical PTI pathways are challenged by pathogen effectors. Future studies dissecting SGN3-dependent phosphorylation events and downstream signaling specificity will further illuminate how developmental and immune programs are dynamically integrated to maintain plant integrity.

Methods

Plant materials and growth conditions

Arabidopsis thaliana (ecotype Columbia, Col-0) plants were grown at 23°C under long-day conditions (16-h light/8-h dark cycle) for general growth and under short-day conditions (8-h light/16-h dark cycle) for pathogen infection assays. The mutant lines used in this study include *sgn3-4* (*gso1-1*; SALK_064029), *gso1-2* (SALK_043539), *gso2-1* (SALK_130637), *gso2-2* (SALK_147249), *pepr1-1/2-1* (Yamaguchi et al., 2010), *pepr1-2/2-2* (Yamaguchi et al., 2010), *cif1-1* (SALK_105801), *cif2-1* (SALK_138660), *cif1 cif2* (Fujita et al., 2020), *cif3 cif4* (Okuda et al., 2020), *cif1 cif2 cif3 cif4* (Okuda et al., 2020), *sgn1-2* (SALK_055095), *bik1*

(SALK_005291), *fls2* (SALK_141277), *fec* (Yuan et al., 2021a), *bbc* (Yuan et al., 2021a), *rpm1-3/rps2-101c* (Mindrinos et al., 1994), and DEX:AvrRpm1-HA (Nimchuk et al., 2000). Homozygous lines were identified by PCR-based genotyping and sequence analysis using gene-specific primers (Supplementary Table 1). To generate $SGN3^{WT}$-eGFP *sgn3-4* and $SGN3^{K979E}$-eGFP *sgn3-4* plants, *SGN3* coding sequence was cloned into the pCAMBIA1300 binary vector fused to an *eGFP* gene under the control of the Cauliflower mosaic virus 35S promoter. The $SGN3^{K979E}$ construct was generated by site-directed mutagenesis using primers in Supplementary Table 1. The resulting constructs were introduced into *Agrobacterium tumefaciens* GV3101 and transformed into the *sgn3-4* mutant by the floral dip method (Clough and Bent, 1998). $SGN3^{WT}$-eGFP *sgn3-4 bik1* plants were generated by crossing $SGN3^{WT}$-eGFP *sgn3-4* lines with the *bik1* mutant and selected by PCR-based genotyping and hygromycin resistance (15 μg ml^{-1}).

Plant treatments

For bacterial pathogen inoculation, *Pst* DC3000 strains were grown at 28°C on NYG agar medium containing rifampicin (50 μg ml^{-1}) and kanamycin (50 μg ml^{-1}) for *Pst* DC3000 and *Pst* DC3000 (*AvrRpm1*) or rifampicin (50 μg ml^{-1}) for *Pst* DC3000 *hrcC*$^-$. Bacteria were harvested and resuspended either in 10 mM $MgCl_2$ for syringe inoculation or in distilled water containing 0.025% (w/v) Silwet L-77 for flood inoculation. For syringe inoculation, 6-week-old leaves were infiltrated with bacterial suspensions at 1×10^6 colony-forming units (CFU) ml^{-1} ($OD_{600} = 0.001$) for bacterial growth assays or 1×10^8 CFU ml^{-1} ($OD_{600} = 0.1$) for other experiments. For flood inoculation, 12-day-old seedlings were submerged in bacterial suspensions at 1×10^8 CFU ml^{-1} ($OD_{600} = 0.1$). For peptide treatments, the flg22 peptide was purchased commercially (Eurogentec) and all other peptides were synthesized through a custom service (GL Biochem). Peptide identity and purity were confirmed by mass

spectrometry and high-performance liquid chromatography. The sequences of the synthesized peptides are as follows (sY, sulfated Y): CIF1, D(sY)GNNSPSPRLERPPFKLIPN; CIF2, D(sY)GHSSPKPKLVRPPFKLIPN; CIF3, D(sY)GSWSPTPKIPRRSPAPIPH; CIF4, D(sY)GFWNPSPVYGGGFPYPGPVPH; CIF2^{I81D}, D(sY)GHSSPKPKLVRPPFKLDPN; and Pep1, ATKVKAKQRGKEKVSSGRPGQHN. All peptides were dissolved in distilled water to prepare 1 mM stock solutions. For leaf assays, peptides were added to bacterial suspensions at a final concentration of 1 μM and co-infiltrated into 6-week-old leaves. For seedling assays, 12-day-old seedlings were transferred to 1/2 Murashige and Skoog (MS) liquid medium supplemented with 1 μM peptide and incubated for 3 days.

Bacterial growth assay

Bacterial growth was determined, as previously described (Lee et al., 2019; Yuan and Xin, 2021). Leaves of 6-week-old plants were syringe-infiltrated with bacterial suspensions at 1×10^6 CFU ml^{-1} (OD_{600} = 0.001). At the indicated time points, 2 leaf discs (3 mm in diameter) were pooled and ground in 10 mM $MgCl_2$ as one replicate. To determine CFU, serial dilutions were plated on NYG agar medium, and bacterial colonies were counted using a stereomicroscope (Zeiss Axio Zoom V16). Experiments were repeated 5 times with biologically independent samples.

Gene expression analysis

Total RNAs were isolated using TRI Reagent (Molecular Research Center) and reverse-transcribed into cDNAs using PrimeScript™ RT Reagent Kit (TaKaRa). Quantitative real-time PCR (RT-qPCR) was performed with THUNDERBIRD™ SYBR™ qPCR Mix (Toyobo) and gene-specific primers (Supplementary Table 1) on a CFX384 real-time PCR detection system (Bio-Rad). *ACTIN2* (AT3G18780) was used as a reference gene for normalization. Data were

analyzed with CFX Maestro software (Bio-Rad). All experiments were repeated 3-5 times with at least 3 biologically independent samples.

Phloroglucinol staining

Lignin deposition was visualized by phloroglucinol staining, as previously described (Lee et al., 2019). Leaves and seedlings were first dehydrated in 100% ethanol overnight, rehydrated through a graded ethanol series (75%, 50%, 25%, and 10%) and distilled water for 30 min each, and subsequently stained for 1 min with 3% (w/v) phloroglucinol (Sigma-Aldrich) dissolved in 30% (v/v) HCl. Stained samples were examined under an optical microscope (Leica EZ4E). Digital images were acquired and analyzed using ImageJ software (NIH) to quantify signal intensity corresponding to lignin deposition in seedlings.

Lignin quantification

Lignin content was quantified using the acetyl bromide soluble lignin (ABSL) method, as previously described (Lee et al., 2019). Pathogen-inoculated leaves were finely ground in liquid nitrogen. Dried tissue samples (3 ± 1 mg, accurately weighed) were sequentially washed with 70% (v/v) ethanol, chloroform:methanol (1:1, v/v), and acetone. The resulting pellets were fully dried at 45°C and digested in 25% (v/v) acetyl bromide in acetic acid at 70°C for 1 h, with vortexing every 10 min. After digestion, samples were cooled on ice and centrifuged at 16,000 *g* for 5 min. Aliquots of the supernatant (100 µl) were transferred to glass tubes and mixed with 400 µl of 2 M NaOH, 70 µl of 0.5 M hydroxylamine hydrochloride, and 430 µl of acetic acid. The mixtures were transferred to 96-well microplates, and absorbance was measured at 280 nm using a microplate reader (Molecular Devices, SpectraMax i3x). Lignin content was calculated according to Beer's Law (Kapp et al., 2015) using an extinction coefficient of 15.69 $l\ g^{-1}\ cm^{-1}$, as determined for *Arabidopsis* (Foster et al., 2010).

562

563 **Protoplast isolation and transfection**

564 *Arabidopsis* mesophyll protoplasts were isolated from rosette leaves of 5-week-old plants, as
565 previously described (Yoo et al., 2007). Leaves were cut into 0.5-1 mm strips and incubated for
566 3 h in enzyme solution (20 mM MES-KOH, pH 5.7, 1% (w/v) cellulase R-10, 0.4% (w/v)
567 macerozyme R-10, 0.4 M D-mannitol, 20 mM KCl, 10 mM $CaCl_2$, and 0.1 % (w/v) BSA), with
568 gentle shaking in the dark. Released protoplasts were filtered through a 70-μm nylon mesh and
569 collected by centrifugation at 100 *g* for 2 min. The pellet was gently resuspended in W5
570 solution (1.5 mM MES-KOH, pH 5.6, 154 mM NaCl, 125 mM $CaCl_2$, and 5 mM KCl).
571 Protoplast transfection was carried out using a polyethylene glycol (PEG)-mediated method,
572 as previously described (Yoo et al., 2007).

573

574 **Bimolecular fluorescence complementation (BiFC) assay**

575 To generate the BiFC constructs, the coding sequences of *SGN3* and *BIK1* were PCR-amplified
576 using gene-specific primers (Supplementary Table 1). The PCR products were cloned into the
577 pUC-SPYNE and pUC-SPYCE vectors to generate fusion constructs encoding SGN3 and
578 BIK1 fused to the N-terminal (YFP^N) or C-terminal (YFP^C) fragments of YFP, yielding SGN3-
579 YFP^N, SGN3-YFP^C, BIK1-YFP^N, and BIK1-YFP^C. *Arabidopsis* mesophyll protoplasts were
580 co-transfected with the indicated BiFC construct combinations and incubated for 20-24 h to
581 allow protein expression. Fluorescence signals were detected using a confocal microscope
582 (Zeiss LSM 700). Excitation and emission were set at 488 and 510 nm for YFP, and 639 and
583 710 nm for chlorophyll.

584

585 **Immunoblotting and co-immunoprecipitation**

586 For immunoblotting, total proteins were extracted by boiling protoplasts in 4× SDS sample

buffer (200 mM Tris–HCl, pH 6.5, 40% glycerol, 8% SDS, 400 mM DTT, and 6 mM bromophenol blue) for 10 min. For immunoprecipitation, protoplasts were lysed in GTEN buffer (25 mM Tris-HCl, pH 7.5, 150 mM NaCl, 1 mM EDTA, 10% glycerol, 1% NP-40, 10 mM DTT, 2 mM NaF, 2 mM Na_3VO_4, and 1× protease inhibitor cocktail) at 4°C with gentle rotation for 30 min. Lysates were centrifuged at 16,000 *g* for 10 min at 4°C, and the supernatants were incubated with anti-HA antibody (Invitrogen) for 1 h at 4°C. Protein A agarose beads (Thermo Scientific) were then added, followed by overnight incubation at 4 °C with rotation. Beads were washed 3 times with washing buffer (25 mM Tris-HCl, pH 7.5, and 150 mM NaCl), and bound proteins were eluted by boiling in 4× SDS sample buffer for 10 min. Proteins were separated by SDS-PAGE and transferred to polyvinylidene fluoride membranes. Membranes were probed with anti-GFP (Santa Cruz Biotechnology), anti-HA (Santa Cruz Biotechnology; Invitrogen), and anti-BIK1 (Agrisera) antibodies, followed by incubation with horseradish peroxidase–conjugated secondary antibodies. Immunoreactive signals were detected using an enhanced chemiluminescence (ECL) system (Amersham Biosciences).

Recombinant protein expression and purification

The full-length coding sequence of *BIK1* and the kinase domain of *SGN3* were PCR-amplified using gene-specific primers (Supplementary Table 1) and cloned into the pGEX-6P-1 and pET-15b vectors, respectively. Constructs of kinase-dead variants ($BIK1^{K105E}$ and SGN3 KD^{K979E}) and $BIK1^{K105E}$ phosphosite mutants (S89A/T90A, Y150F, S236A, T237A, S236A/T237A, T242A, Y243F, and Y250F) were generated by site-directed mutagenesis using primers in Supplementary Table 1. Recombinant protein expression was performed, as previously described (Lee et al., 2017), with minor modifications. *Escherichia coli* BL21(DE3) pLysS cells were transformed with the constructs and cultured at 37°C. Protein expression was induced by the addition of 100 μM isopropyl-β-D-thiogalactoside (IPTG), followed by

612 incubation overnight at 18°C. GST- and His-tagged proteins were purified using Glutathione
613 Sepharose 4B (Cytiva) and Ni^{2+}-NTA agarose (Qiagen) beads, respectively, according to the
614 manufacturer's instructions.
615
616 **GST pull-down assay**
617 GST pull-down assays were performed, as previously described (Lee et al., 2017), with minor
618 modifications. GST or GST-fused BIK1 (5 μg) was incubated with His-tagged SGN3 KD (5
619 μg) in binding buffer (20 mM Tris-HCl, pH 7.4, 200 mM NaCl, and 1 mM EDTA) for 2 h at
620 4°C. Glutathione Sepharose 4B beads (Cytiva) were added, incubated for an additional 2 h, and
621 washed 3 times with washing buffer (20 mM Tris-HCl, pH 7.4, 200 mM NaCl, 1 mM EDTA,
622 and 0.5% Triton X-100). Bound proteins were eluted by boiling the beads in 4× SDS sample
623 buffer, separated by SDS-PAGE, and visualized by immunoblotting using anti-GST and anti-
624 His antibodies (Santa Cruz Biotechnology).
625
626 ***In vitro* kinase assay**
627 In vitro kinase assays were performed, as previously described (Alassimone et al., 2016; Fujita
628 et al., 2020), with minor modifications. Purified His-SGN3 KD^{WT} or His-SGN3 KD^{K979E} (1
629 μg) was incubated with GST-$BIK1^{K105E}$ or GST-$BIK1^{K105E}$ phosphosite mutant proteins (1 μg)
630 in kinase reaction buffer (50 mM HEPES-KOH, pH 8.0, 1 mM $MnCl_2$, 1 mM DTT, 1 mM ATP,
631 and 20 μCi [γ-^{32}P] ATP) at room temperature for 2 h. Reactions were terminated by boiling the
632 samples in 4× SDS sample buffer for 10 min. Proteins were separated by SDS-PAGE on 10%
633 polyacrylamide gels. After drying gels, radioactive signals were detected by autoradiography.
634
635 **Rapamycin-inducible dimerization (RiD) assay**
636 RiD assays were performed, as described previously (Kim et al., 2021). *Nicotiana benthamiana*

637 (Nb-1) leaves were transiently transformed with *A. tumefaciens* GV3101 carrying RiD
638 constructs encoding FLS2 KD-FKBP, SGN3 KD-FKBP, BAK1 KD-FRB, BIK1-GFP, and
639 SGN1-GFP. *A. tumefaciens* cultures were grown to OD_{600} of 0.7, harvested, and resuspended
640 in infiltration medium (10 mM MES-KOH, pH 5.6, 10 mM $MgCl_2$, and 0.15 mM
641 acetosyringone). Cell suspensions were syringe-infiltrated into *N. benthamiana* leaves, which
642 were then incubated for 72 h under standard growth conditions. Agroinfiltrated leaves were
643 vacuum-infiltrated with 1 μM rapamycin (Cayman Chemical) containing 0.01% (w/v) Silwet
644 L-77. Total proteins were extracted by boiling leaf tissues in 4× SDS sample buffer and
645 analyzed by immunoblotting using anti-GFP (TaKaRa), anti-HA (Santa Cruz Biotechnology),
646 and anti-Myc (Cell Signaling) antibodies.
647
648 **Microscopy analysis**
649 For bacterial localization, leaves were syringe-infiltrated with GFP-labeled *Pst* DC3000
650 (*AvrRpt2*) at 1×10^8 CFU ml^{-1} ($OD_{600} = 0.1$) and analyzed at 2 days post-inoculation. For ROS
651 production, leaves were syringe-infiltrated with *Pst* DC3000 (*AvrRpm1*) at 1×10^8 CFU ml^{-1}
652 ($OD_{600} = 0.1$) and analyzed at 16 h post-inoculation. Inoculated leaves were vacuum-infiltrated
653 with 10 μM H_2DCFDA (Invitrogen) for 10 min and washed 5 times with distilled water prior
654 to imaging. For lignin localization, leaves were pre-treated with either coniferyl alcohol (CA;
655 50 μM) or a CADMAC (Tobimatsu et al., 2013) mixture (100 μM CA and 1 μM CADMAC),
656 air-dried, and then inoculated with *Pst* DC3000 (*AvrRpm1*) at 1×10^6 CFU ml^{-1}
657 ($OD_{600} = 0.001$). GFP, DCF, and CADMAC signals were observed using a confocal microscope
658 (Zeiss LSM800). Excitation and emission were set at 405 and 490 nm for CADMAC, 488 and
659 510 nm for GFP and DCF, and 639 and 710 nm for chlorophyll.
660
661 **Statistical analysis**

Statistical analyses were performed using GraphPad Prism (v. 10.6). Data were presented as mean ± standard deviation. Significant differences between experimental groups were evaluated by one-way ANOVA with Tukey's HSD test for multiple comparisons or unpaired Student's *t* test for single comparisons. Statistical significance was set at $P < 0.05$. Detailed information about statistical analysis is described in the figure legends. All experiments were repeated at least 3 times with similar results.

Acknowledgements

We thank Niko Geldner for *cif1 cif2*, *cif3 cif4*, and *cif1 cif2 cif3 cif4* seeds, Frans Tax for *gso1* and *gso2* seeds, Yube Yamaguchi for *pepr1*, *pepr2*, and *pepr1*/*2* seeds, and Xiu-Fang Xin and Cyril Zipfel for *fec* and *bbc* seeds. We are also grateful to Niko Geldner for technical advice and critical reading of the manuscript. This work was supported by a Korea University grant and National Research Foundation of Korea (NRF) grants (RS-2024-00339452, RS-2024-00351755, RS-2025-00512558) from the Korean government (MSIP).

Author contributions

O.K.P. conceived and supervised the project. E.J., H.S.J., and O.K.P. designed the research. E.J. and H.S.J. performed most of the experiments. M.A. participated in protoplast transient expression assays, H.C. performed RiD assays, and S.J. and M.T.S. participated in BIK1 mutant construction and kinase assays. E.J., H.S.J., and O.K.P. analyzed the data and wrote the manuscript. Y.T. and E.O. provided materials and contributed to critical discussion of the work. All authors reviewed and edited the manuscript.

Competing interests

The authors declare no competing interests.

687 **References**

688

689 Adams-Phillips, L., Briggs, A. G. & Bent, A. F. Disruption of poly (ADP-ribosyl)ation
690 mechanisms alters responses of *Arabidopsis* to biotic stress. *Plant Physiol.* **152**, 267–
691 280 (2009).
692 Alassimone, J. et al. Polarly localized kinase SGN1 is required for Casparian strip integrity and
693 positioning. *Nat. Plants* **2**, 1–10 (2016).
694 Alejandro, S. et al. AtABCG29 is a monolignol transporter involved in lignin biosynthesis.
695 *Curr. Biol.* **22**, 1207–1212 (2012).
696 Andreasson, E. & Ellis, B. Convergence and specificity in the *Arabidopsis* MAPK nexus.
697 *Trends Plant Sci.* **15**, 106–113 (2010).
698 Barros, J., Serk, H., Granlund, I. & Pesquet, E. The cell biology of lignification in higher plants.
699 *Ann. Bot.* **115**, 1053–1074 (2015).
700 Bartels, S. & Boller, T. Quo vadis, Pep? Plant elicitor peptides at the crossroads of immunity,
701 stress, and development. *J. Exp. Bot.* **66**, 5183–5193 (2015).
702 Bi, G. et al. Receptor-like cytoplasmic kinases directly link diverse pattern recognition
703 receptors to the activation of mitogen-activated protein kinase cascades in *Arabidopsis*.
704 *Plant Cell* **30**, 1543–1561 (2018).
705 Boller, T. & Felix, G. A renaissance of elicitors: perception of microbe-associated molecular
706 patterns and danger signals by pattern-recognition receptors. *Annu. Rev. Plant Biol.* **60**,
707 379–406 (2009).
708 Cao, Y. et al. Mutations in FLS2 Ser-938 dissect signaling activation in FLS2-mediated
709 *Arabidopsis* immunity. *PLoS Pathog.* **9**, e1003313 (2013).
710 Cesarino, I. Structural features and regulation of lignin deposited upon biotic and abiotic
711 stresses. *Curr. Opin. Biotechnol.* **56**, 209–214 (2019).

712 Chang, M., Chen, H., Liu, F. & Fu, Z. Q. PTI and ETI: convergent pathways with diverse
713 elicitors. *Trends Plant Sci.* **27**, 113–115 (2022).
714 Chezem, W. R., Memon, A., Li, F.-S., Weng, J.-K. & Clay, N. K. SG2-type R2R3-MYB
715 transcription factor MYB15 controls defense-induced lignification and basal immunity
716 in *Arabidopsis*. *Plant Cell* **29**, 1907–1926 (2017).
717 Chinchilla, D. et al. A flagellin-induced complex of the receptor FLS2 and BAK1 initiates plant
718 defence. *Nature* **448**, 497–500 (2007).
719 Cho, H., Lee, J. & Oh, E. Leucine-rich repeat receptor-like proteins in plants: structure,
720 function, and signaling. *J. Plant Biol.* **66**, 99–107 (2023).
721 Choi, H. W. & Klessig, D. F. DAMPs, MAMPs, and NAMPs in plant innate immunity. *BMC*
722 *Plant Biol.* **16**, 1–10 (2016).
723 Clough, S. J. & Bent, A. F. Floral dip: a simplified method for *Agrobacterium*-mediated
724 transformation of *Arabidopsis thaliana*. *Plant J.* **16**, 735–743 (1998).
725 Couto, D. & Zipfel, C. Regulation of pattern recognition receptor signalling in plants. *Nat. Rev.*
726 *Immunol.* **16**, 537–552 (2016).
727 Cui, F., Sun, W. & Kong, X. RLCKs bridge plant immune receptors and MAPK cascades.
728 *Trends Plant Sci.* **23**, 1039–1041 (2018).
729 Doblas, V. G. et al. Root diffusion barrier control by a vasculature-derived peptide binding to
730 the SGN3 receptor. *Science* **355**, 280–284 (2017).
731 Doll, N. et al. A two-way molecular dialogue between embryo and endosperm is required for
732 seed development. *Science* **367**, 431–435 (2020).
733 Engelsdorf, T. et al. The plant cell wall integrity maintenance and immune signaling systems
734 cooperate to control stress responses in *Arabidopsis thaliana*. *Sci. Signal.* **11**, eaao3070
735 (2018).
736 Foster, C. E., Martin, T. M. & Pauly, M. Comprehensive compositional analysis of plant cell

walls (lignocellulosic biomass) part I: lignin. *J. Vis. Exp.*, e1745 (2010).

Fujita, S. et al. SCHENGEN receptor module drives localized ROS production and lignification in plant roots. *EMBO J.* **39**, e103894 (2020).

Gao, Y.-Q. et al. A dirigent protein complex directs lignin polymerization and assembly of the root diffusion barrier. *Science* **382**, 464–471 (2023).

Göhre, V. et al. Plant pattern-recognition receptor FLS2 is directed for degradation by the bacterial ubiquitin ligase AvrPtoB. *Curr. Biol.* **18**, 1824–1832 (2008).

Hou, S., Liu, Z., Shen, H. & Wu, D. Damage-associated molecular pattern-triggered immunity in plants. *Front. Plant Sci.* **10**, 646 (2019).

Huh, S. U. et al. Protein-protein interactions in the RPS4/RRS1 immune receptor complex. *PLoS Pathog.* **13**, e1006376 (2017).

Jeon, H. S. et al. Pathogen-induced autophagy regulates monolignol transport and lignin formation in plant immunity. *Autophagy* **19**, 597–615 (2023).

Jiang, Y. et al. MAP 4k4 associates with BIK 1 to regulate plant innate immunity. *EMBO Rep.* **20**, e47965 (2019).

Kapp, N., Barnes, W. J., Richard, T. L. & Anderson, C. T. Imaging with the fluorogenic dye Basic Fuchsin reveals subcellular patterning and ecotype variation of lignification in *Brachypodium distachyon*. *J. Exp. Bot.* **66**, 4295-4304 (2015).

Kim, S. et al. Chemical control of receptor kinase signaling by rapamycin-induced dimerization. *Mol. Plant* **14**, 1379–1390 (2021).

Kim, S. H. et al. The *Arabidopsis* R2R3 MYB transcription factor MYB15 is a key regulator of lignin biosynthesis in effector-triggered immunity. *Front. Plant Sci.* **11**, 583153 (2020).

Lal, N. K. et al. The receptor-like cytoplasmic kinase BIK1 localizes to the nucleus and regulates defense hormone expression during plant innate immunity. *Cell Host Microbe*

23, 485–497 (2018).

Lee, D. S., Kim, Y. C., Kwon, S. J., Ryu, C.-M. & Park, O. K. The *Arabidopsis* cysteine-rich receptor-like kinase CRK36 regulates immunity through interaction with the cytoplasmic kinase BIK1. *Front. Plant Sci.* **8**, 1856 (2017).

Lee, M. H. et al. Lignin-based barrier restricts pathogens to the infection site and confers resistance in plants. *EMBO J.* **38**, e101948 (2019).

Lee, Y., Rubio, M. C., Alassimone, J. & Geldner, N. A mechanism for localized lignin deposition in the endodermis. *Cell* **153**, 402–412 (2013).

Li, L. et al. The FLS2-associated kinase BIK1 directly phosphorylates the NADPH oxidase RbohD to control plant immunity. *Cell Host Microbe* **15**, 329–338 (2014).

Li, X., Kapos, P. & Zhang, Y. NLRs in plants. *Curr. Opin. Immunol.* **32**, 114–121 (2015).

Lin, W. et al. Tyrosine phosphorylation of protein kinase complex BAK1/BIK1 mediates *Arabidopsis* innate immunity. *Proc. Natl Acad. Sci. USA* **111**, 3632–3637 (2014).

Liu, Q., Luo, L. & Zheng, L. Lignins: biosynthesis and biological functions in plants. *Int. J. Mol. Sci.* **19**, 335 (2018).

Liu, Z. et al. BIK1 interacts with PEPRs to mediate ethylene-induced immunity. *Proc. Natl Acad. Sci. USA* **110**, 6205–6210 (2013).

Lu, D. et al. A receptor-like cytoplasmic kinase, BIK1, associates with a flagellin receptor complex to initiate plant innate immunity. *Proc. Natl Acad. Sci. USA* **107**, 496–501 (2010).

Ma, Q.-H. Lignin biosynthesis and its diversified roles in disease resistance. *Genes* **15**, 295 (2024).

Ma, Y. et al. Comparisons of two receptor-MAPK pathways in a single cell-type reveal mechanisms of signalling specificity. *Nat. Plants* **10**, 1343–1362 (2024).

Ma, Y. & Nicolet, J. Specificity models in MAPK cascade signaling. *FEBS Open Bio* **13**, 1177–

1192 (2023).

Malinovsky, F. G., Fangel, J. U. & Willats, W. G. The role of the cell wall in plant immunity. *Front. Plant Sci.* **5**, 178 (2014).

Mindrinos, M., Katagiri, F., Yu, G.-L. & Ausubel, F. M. The *A. thaliana* disease resistance gene *RPS2* encodes a protein containing a nucleotide-binding site and leucine-rich repeats. *Cell* **78**, 1089–1099 (1994).

Molina, A. et al. Plant cell wall-mediated disease resistance: Current understanding and future perspectives. *Mol. Plant* **17**, 699–724 (2024).

Nakayama, T. et al. A peptide hormone required for Casparian strip diffusion barrier formation in *Arabidopsis* roots. *Science* **355**, 284–286 (2017).

Naseer, S. et al. Casparian strip diffusion barrier in *Arabidopsis* is made of a lignin polymer without suberin. *Proc. Natl Acad. Sci. USA* **109**, 10101–10106 (2012).

Ngou, B. P. M., Ahn, H.-K., Ding, P. & Jones, J. D. Mutual potentiation of plant immunity by cell-surface and intracellular receptors. *Nature* **592**, 110–115 (2021).

Nimchuk, Z. et al. Eukaryotic fatty acylation drives plasma membrane targeting and enhances function of several type III effector proteins from *Pseudomonas syringae*. *Cell* **101**, 353–363 (2000).

Okuda, S. et al. Molecular mechanism for the recognition of sequence-divergent CIF peptides by the plant receptor kinases GSO1/SGN3 and GSO2. *Proc. Natl Acad. Sci. USA* **117**, 2693–2703 (2020).

Pfister, A. et al. A receptor-like kinase mutant with absent endodermal diffusion barrier displays selective nutrient homeostasis defects. *eLife* **3**, e03115 (2014).

Pruitt, R. N. et al. The EDS1–PAD4–ADR1 node mediates *Arabidopsis* pattern-triggered immunity. *Nature* **598**, 495–499 (2021).

Racolta, A., Bryan, A. C. & Tax, F. E. The receptor-like kinases GSO1 and GSO2 together

812 regulate root growth in *Arabidopsis* through control of cell division and cell fate
813 specification. *Dev. Dyn.* **243**, 257–278 (2014).
814 Rojas-Murcia, N. et al. High-order mutants reveal an essential requirement for peroxidases but
815 not laccases in Casparian strip lignification. *Proc. Natl Acad. Sci. USA* **117**, 29166–
816 29177 (2020).
817 Roppolo, D. et al. A novel protein family mediates Casparian strip formation in the endodermis.
818 *Nature* **473**, 380–383 (2011).
819 Shan, L. et al. Bacterial effectors target the common signaling partner BAK1 to disrupt multiple
820 MAMP receptor-signaling complexes and impede plant immunity. *Cell Host Microbe*
821 **4**, 17–27 (2008).
822 Sibout, R. & Höfte, H. Plant cell biology: the ABC of monolignol transport. *Curr. Biol.* **22**,
823 R533–R535 (2012).
824 Sun, Y. et al. Structural basis for flg22-induced activation of the *Arabidopsis* FLS2-BAK1
825 immune complex. *Science* **342**, 624–628 (2013).
826 Tian, H. et al. Activation of TIR signalling boosts pattern-triggered immunity. *Nature* **598**,
827 500–503 (2021).
828 Tobimatsu, Y. & Schuetz, M. Lignin polymerization: how do plants manage the chemistry so
829 well? *Curr. Opin. Biotechnol.* **56**, 75–81 (2019).
830 Truskina, J. et al. A peptide-mediated, multilateral molecular dialogue for the coordination of
831 pollen wall formation. *Proc. Natl Acad. Sci. USA* **119**, e2201446119 (2022).
832 Tsuwamoto, R., Fukuoka, H. & Takahata, Y. GASSHO1 and GASSHO2 encoding a putative
833 leucine-rich repeat transmembrane-type receptor kinase are essential for the normal
834 development of the epidermal surface in *Arabidopsis* embryos. *Plant J.* **54**, 30–42
835 (2008).
836 Vanholme, R., De Meester, B., Ralph, J. & Boerjan, W. Lignin biosynthesis and its integration

837 into metabolism. *Curr. Opin. Biotechnol.* **56**, 230–239 (2019).
838 Wang, F.-L. et al. A potassium-sensing niche in *Arabidopsis* roots orchestrates signaling and
839 adaptation responses to maintain nutrient homeostasis. *Dev. Cell* **56**, 781–794 (2021).
840 Wang, J. et al. Reconstitution and structure of a plant NLR resistosome conferring immunity.
841 *Science* **364**, eaav5870 (2019).
842 Xiang, T. et al. *Pseudomonas syringae* effector AvrPto blocks innate immunity by targeting
843 receptor kinases. *Curr. Biol.* **18**, 74–80 (2008).
844 Yamaguchi, Y., Huffaker, A., Bryan, A. C., Tax, F. E. & Ryan, C. A. PEPR2 is a second
845 receptor for the Pep1 and Pep2 peptides and contributes to defense responses in
846 *Arabidopsis*. *Plant Cell* **22**, 508–522 (2010).
847 Yao, T. et al. Phylogenetic occurrence of the phenylpropanoid pathway and lignin biosynthesis
848 in plants. *Front. Plant Sci.* **12**, 704697 (2021).
849 Yoo, S.-D., Cho, Y.-H. & Sheen, J. *Arabidopsis* mesophyll protoplasts: a versatile cell system
850 for transient gene expression analysis. *Nat. Protoc.* **2**, 1565–1572 (2007).
851 Yuan, M. et al. Pattern-recognition receptors are required for NLR-mediated plant immunity.
852 *Nature* **592**, 105–109 (2021a).
853 Yuan, M., Ngou, B. P. M., Ding, P. & Xin, X.-F. PTI-ETI crosstalk: an integrative view of
854 plant immunity. *Curr. Opin. Plant Biol.* **62**, 102030 (2021b).
855 Yuan, M. & Xin, X.-F. Bacterial infection and hypersensitive response assays in *Arabidopsis*-
856 *Pseudomonas syringae* pathosystem. *Bio Protoc.* **11**, e4268 (2021).
857 Zhang, H. et al. SERKs regulate embryonic cuticle integrity through the TWS1-GSO1/2
858 signaling pathway in *Arabidopsis*. *New Phytol.* **233**, 313–328 (2022a).
859 Zhang, J. et al. Receptor-like cytoplasmic kinases integrate signaling from multiple plant
860 immune receptors and are targeted by a *Pseudomonas syringae* effector. *Cell Host*
861 *Microbe* **7**, 290–301 (2010).

862 Zhang, J., Li, Y., Bao, Q., Wang, H. & Hou, S. Plant elicitor peptide 1 fortifies root cell walls
863 and triggers a systemic root-to-shoot immune signaling in *Arabidopsis*. *Plant Signal.*
864 *Behav.* **17**, 2034270 (2022b).
865 Zhang, S., Yang, J., Li, H., Chiang, V. L. & Fu, Y. Cooperative regulation of flavonoid and
866 lignin biosynthesis in plants. *Crit. Rev. Plant Sci.* **40**, 109–126 (2021).
867 Zipfel, C. Plant pattern-recognition receptors. *Trends Immunol.* **35**, 345–351 (2014).
868 Zipfel, C. et al. Perception of the bacterial PAMP EF-Tu by the receptor EFR restricts
869 *Agrobacterium*-mediated transformation. *Cell* **125**, 749–760 (2006).

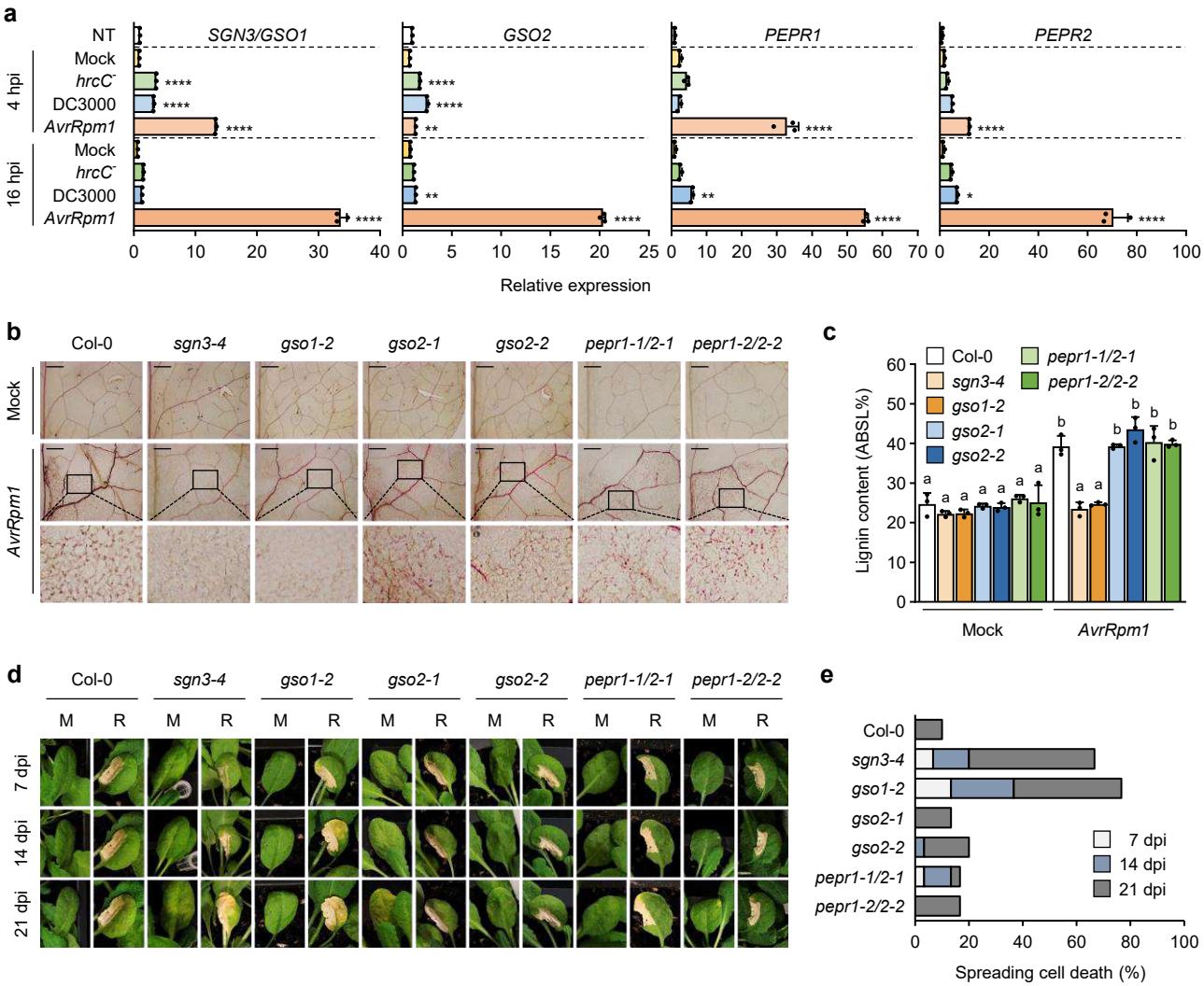

a
NT
Mock
hrcC-
DC3000
AvrRpm1
4 hpi
16 hpi
SGN3/GSO1
GSO2
PEPR1
PEPR2
Relative expression
b
Col-0
sgn3-4
gso1-2
gso2-1
gso2-2
pepr1-1/2-1
pepr1-2/2-2
Mock
AvrRpm1
c
Lignin content (ABSL%)
Mock
AvrRpm1
d
M
R
7 dpi
14 dpi
21 dpi
e
Spreading cell death (%)

Fig. 1. SGN3/GSO1 is required for ETI-associated lignification.
a, Expression of *SGN3/GSO1*, *GSO2*, *PEPR1*, and *PEPR2* in Col-0 leaves infiltrated with mock or the indicated *Pst* DC3000 strains at 4 and 16 hpi. Data are means ± SD (n = 3). Asterisks indicate significant differences relative to the no-treatment control (NT) (t test; *P < 0.05; **P < 0.01; ****P < 0.0001).
b, Phloroglucinol staining of Col-0, *sgn3*, *gso1*, *gso2*, and *pepr1*/*2* leaves infiltrated with mock or *Pst* DC3000 (*AvrRpm1*) at 2 dpi. Boxed regions are shown at higher magnification below. Scale bars, 500 µm.
c, Quantification of lignin content in leaves as shown in (**b**). Data are means ± SD (n = 3; 3–9 leaves each). Different letters indicate significant differences (Tukey's HSD test; P < 0.05).
d, Cell death phenotypes of Col-0, *sgn3*, *gso1*, *gso2*, and *pepr1*/*2* leaves infiltrated with mock or *Pst* DC3000 (*AvrRpm1*). M, mock; R, *Pst* DC3000 (*AvrRpm1*).
e, Quantification of leaves (n = 30) with spreading cell death as shown in (**d**).
For all experiments, 6-week-old leaves were infiltrated with mock (10 mM $MgCl_2$) or the indicated *Pst* DC3000 strains at 1×10^8 CFU ml^{-1}. *hrcC*$^-$, *Pst* DC3000 *hrcC*$^-$; DC3000, *Pst* DC3000; *AvrRpm1*, *Pst* DC3000 (*AvrRpm1*); hpi, hours post-inoculation; dpi, days post-inoculation.

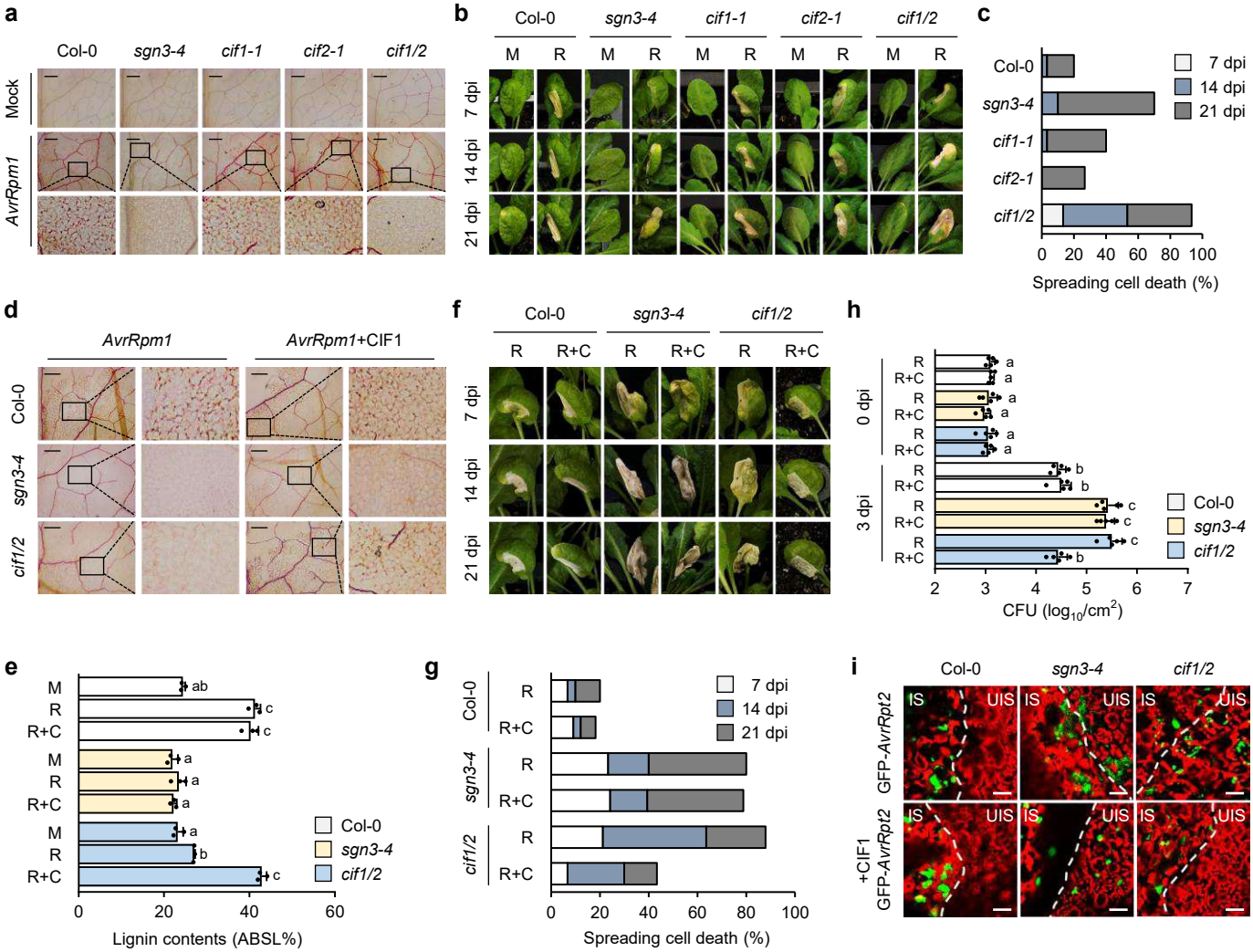

a
Col-0
sgn3-4
cif1-1
cif2-1
cif1/2
Mock
AvrRpm1
b
Col-0
sgn3-4
cif1-1
cif2-1
cif1/2
M
R
7 dpi
14 dpi
21 dpi
c
7 dpi
14 dpi
21 dpi
Spreading cell death (%)
d
AvrRpm1
AvrRpm1+CIF1
e
Lignin contents (ABSL%)
f
R
R+C
g
Spreading cell death (%)
h
0 dpi
3 dpi
CFU (log10/cm2)
i
IS
UIS
GFP-AvrRpt2
+CIF1
GFP-AvrRpt2

Fig. 2. CIF1 and CIF2 serve as primary ligands for SGN3 during ETI.
a, Phloroglucinol staining of Col-0, *sgn3*, *cif1*, *cif2*, and *cif1*/*2* leaves infiltrated with mock or *Pst* DC3000 (*AvrRpm1*) at 2 dpi. Boxed regions are shown at higher magnification below. Scale bars, 500 μm.
b, Cell death phenotypes of Col-0, *sgn3*, *cif1*, *cif2*, and *cif1*/*2* leaves infiltrated with mock or *Pst* DC3000 (*AvrRpm1*).
c, Quantification of leaves (n = 30) with spreading cell death as shown in (**b**).
d, Phloroglucinol staining of Col-0, *sgn3*, and *cif1*/*2* leaves infiltrated with mock or *Pst* DC3000 (*AvrRpm1*) in the presence or absence of CIF1 peptide at 2 dpi. Boxed regions are shown at higher magnification below. *AvrRpm1*, *Pst* DC3000 (*AvrRpm1*). Scale bars, 500 μm.
e, Quantification of lignin content in leaves as shown in (**d**). Data are means ± SD (n = 3; 3–9 leaves each). Different letters indicate significant differences (Tukey's HSD test; $P < 0.05$).
f, Cell death phenotypes of Col-0, *sgn3*, and *cif1*/*2* leaves infiltrated with mock or *Pst* DC3000 (*AvrRpm1*) in the presence or absence of CIF1 peptide.
g, Quantification of leaves ($n \geq 30$) with spreading cell death as shown in (**f**).
h, Bacterial growth of *Pst* DC3000 (*AvrRpm1*) in Col-0, *sgn3*, and *cif1*/*2* leaves in the presence or absence of CIF1 peptide. Data are means ± SD (n = 5). Different letters indicate significant differences (Tukey's HSD test; $P < 0.05$).
i, Colonization patterns of GFP-*Pst* DC3000 (*AvrRpt2*) in Col-0, *sgn3*, and *cif1*/*2* leaves in the presence or absence of CIF1 peptide at 2 dpi. White dotted lines indicate the boundary between infected sites (IS) and adjacent uninfected sites (UIS). Scale bars, 50 μm.
Six-week-old leaves were infiltrated with mock (10 mM $MgCl_2$) or *Pst* DC3000 (*AvrRpm1*) at 1×10^6 CFU ml^{-1} (**h**) or 1×10^8 CFU ml^{-1} (**a**–**g**), or with GFP-*Pst* DC3000 (*AvrRpt2*) at 1×10^8 CFU ml^{-1} (**i**). For peptide treatments, CIF1 was added to bacterial suspensions at a final concentration of 1 μM. M, mock; R, *Pst* DC3000 (*AvrRpm1*); C, CIF1; dpi, days post-inoculation.

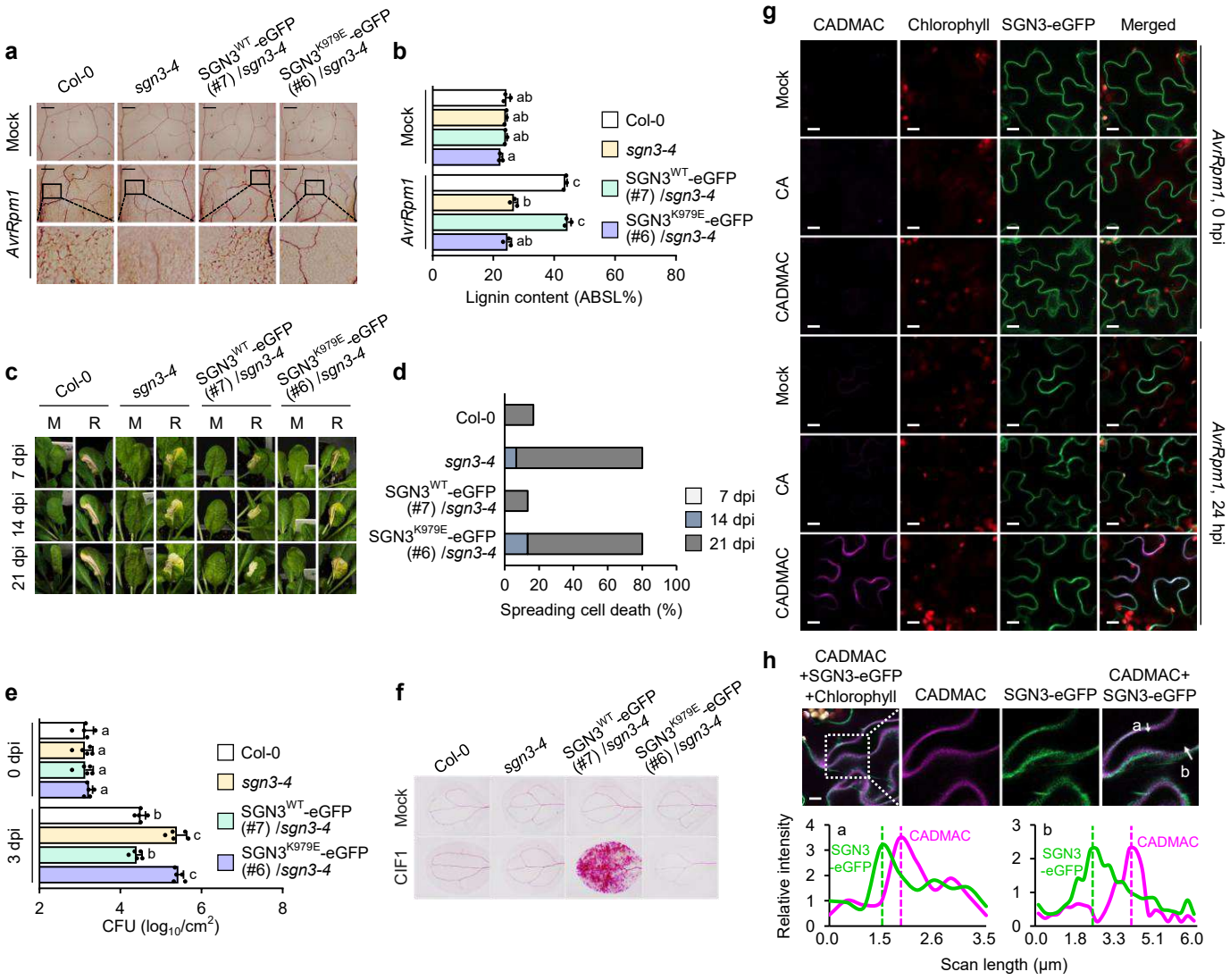

a
Col-0
sgn3-4
SGN3WT-eGFP (#7) /sgn3-4
SGN3K979E-eGFP (#6) /sgn3-4
Mock
AvrRpm1
b
Lignin content (ABSL%)
c
Col-0
sgn3-4
SGN3WT-eGFP (#7) /sgn3-4
SGN3K979E-eGFP (#6) /sgn3-4
M
R
7 dpi
14 dpi
21 dpi
d
Spreading cell death (%)
e
0 dpi
3 dpi
CFU (log10/cm2)
f
CIF1
g
CADMAC
Chlorophyll
SGN3-eGFP
Merged
CA
AvrRpm1, 0 hpi
AvrRpm1, 24 hpi
h
CADMAC +SGN3-eGFP +Chlorophyll
CADMAC+ SGN3-eGFP
Relative intensity
Scan length (μm)

Fig. 3. SGN3 regulates lignin barrier formation in a kinase activity-dependent manner.
a, Phloroglucinol staining of Col-0, *sgn3*, SGN3^{WT}-eGFP/*sgn3*, and SGN3^{K979E}-eGFP/*sgn3* leaves infiltrated with mock or *Pst* DC3000 (*AvrRpm1*) at 2 dpi. Boxed regions are shown at higher magnification below. Scale bars, 500 μm.
b, Quantification of lignin content in leaves as shown in (**a**). Data are means ± SD (n = 3; 3–9 leaves each). Different letters indicate significant differences (Tukey's HSD test; $P < 0.05$).
c, Cell death phenotypes of Col-0, *sgn3*, SGN3^{WT}-eGFP/*sgn3*, and SGN3^{K979E}-eGFP/*sgn3* leaves infiltrated with mock or *Pst* DC3000 (*AvrRpm1*). M, mock; R, *Pst* DC3000 (*AvrRpm1*).
d, Quantification of leaves (n = 30) with spreading cell death as shown in (**c**).
e, Bacterial growth of *Pst* DC3000 (*AvrRpm1*) in Col-0, *sgn3*, SGN3^{WT}-eGFP/*sgn3*, and SGN3^{K979E}-eGFP/*sgn3* leaves. Data are means ± SD (n = 5). Different letters indicate significant differences (Tukey's HSD test; $P < 0.05$).
f, Phloroglucinol staining of Col-0, *sgn3*, SGN3^{WT}-eGFP/*sgn3*, and SGN3^{K979E}-eGFP/*sgn3* seedlings treated with mock or CIF1 peptide for 3 days.
g, Representative microscopic images of CADMAC-incorporated lignin and SGN3-eGFP localization in SGN3^{WT}-eGFP/*sgn3* leaves infiltrated with *Pst* DC3000 (*AvrRpm1*). Scale bars, 10 μm.
h, Relative fluorescence intensity profiles of lignin (CADMAC) and SGN3-eGFP along transects indicated by arrows and letters a and b in the magnified image. Scale bars, 10 μm.
Six-week-old leaves were infiltrated with mock (10 mM $MgCl_2$) or *Pst* DC3000 (*AvrRpm1*) at 1×10^6 CFU ml^{-1} (**e**) or 1×10^8 CFU ml^{-1} (**a**–**d, g, h**). Twelve-day-old seedlings were treated with mock (distilled water) or 1 μM CIF1 peptide (**f**). CA, coniferyl alcohol; CADMAC, dimethylaminocoumarin-coniferyl alcohol; dpi, days post-inoculation.

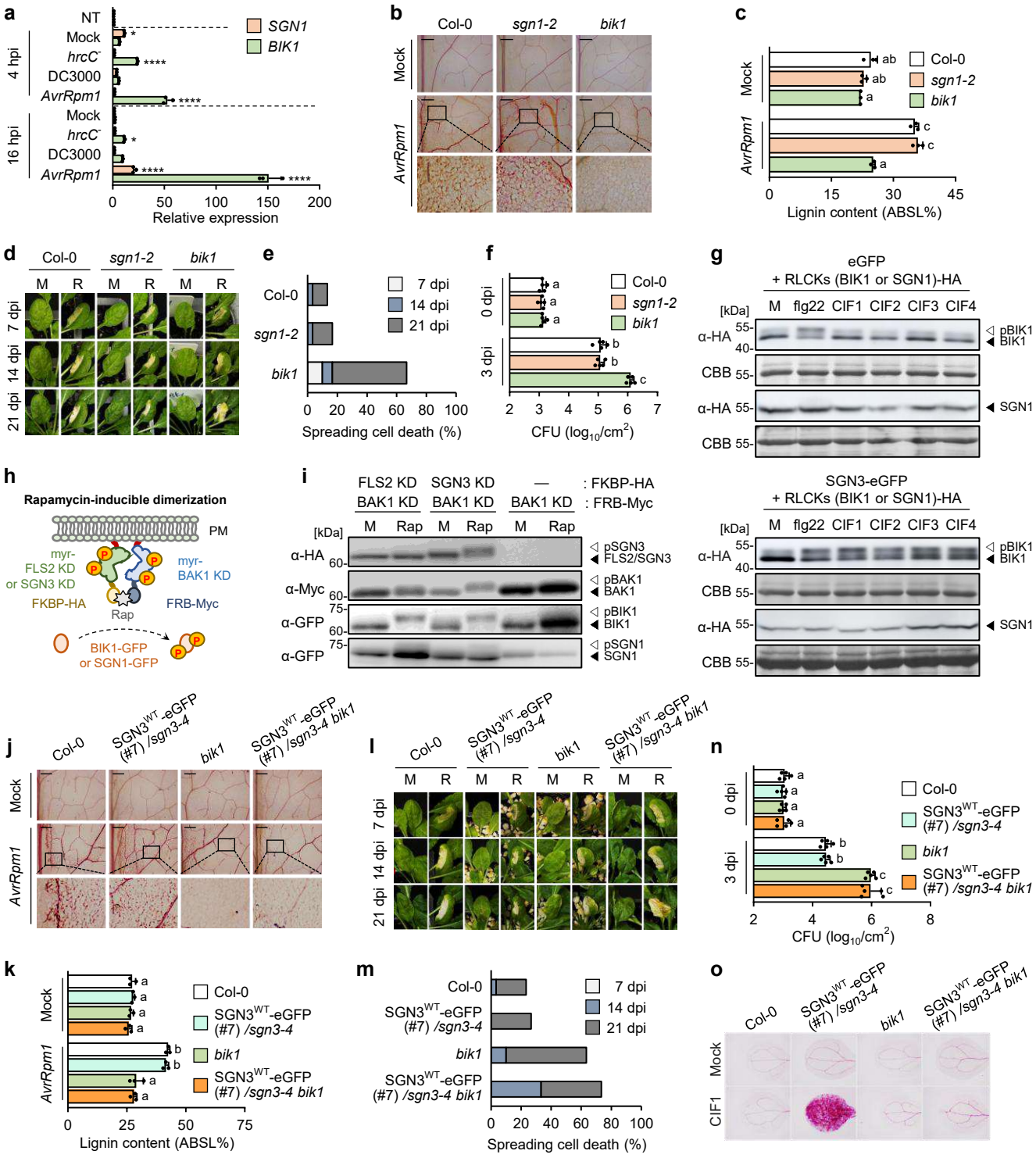

a
NT
Mock
hrcC-
DC3000
AvrRpm1
4 hpi
16 hpi
SGN1
BIK1
Relative expression
b
Col-0
sgn1-2
bik1
Mock
AvrRpm1
c
Lignin content (ABSL%)
d
M
R
7 dpi
14 dpi
21 dpi
e
Spreading cell death (%)
f
0 dpi
3 dpi
CFU (log10/cm2)
g
eGFP
+ RLCKs (BIK1 or SGN1)-HA
M
flg22
CIF1
CIF2
CIF3
CIF4
α-HA
CBB
pBIK1
BIK1
SGN1
SGN3-eGFP
h
Rapamycin-inducible dimerization
PM
myr-
FLS2 KD
or SGN3 KD
FKBP-HA
myr-
BAK1 KD
FRB-Myc
Rap
BIK1-GFP
or SGN1-GFP
i
FLS2 KD
SGN3 KD
BAK1 KD
: FKBP-HA
: FRB-Myc
Rap
α-Myc
α-GFP
pSGN3
FLS2/SGN3
pBAK1
BAK1
pSGN1
SGN1
j
SGN3WT-eGFP
(#7) /sgn3-4
SGN3WT-eGFP
(#7) /sgn3-4 bik1
l
n
SGN3WT-eGFP
(#7) /sgn3-4
SGN3WT-eGFP
(#7) /sgn3-4 bik1
k
m
o

Fig. 4. BIK1 functions downstream of the CIF1/2–SGN3 complex during ETI.

a, Expression of *SGN1* and *BIK1* in Col-0 leaves infiltrated with mock or the indicated *Pst* DC3000 strains at 4 and 16 hpi. Data are means ± SD (n = 3). Asterisks indicate significant differences relative to the no-treatment control (NT) (t test; *P < 0.05; ****P < 0.0001).

b, Phloroglucinol staining of Col-0, *sgn1*, and *bik1* leaves infiltrated with mock or *Pst* DC3000 (*AvrRpm1*) at 2 dpi. Boxed regions are shown at higher magnification below. Scale bars, 500 µm.

c, Quantification of lignin content in leaves as shown in (**b**). Data are means ± SD (n = 3; 3–9 leaves each). Different letters indicate significant differences (Tukey's HSD test; P < 0.05).

d, Cell death phenotypes of Col-0, *sgn1*, and *bik1* leaves infiltrated with mock or *Pst* DC3000 (*AvrRpm1*). M, mock; R, *Pst* DC3000 (*AvrRpm1*).

e, Quantification of leaves (n = 30) with spreading cell death as shown in (**d**).

f, Bacterial growth of *Pst* DC3000 (*AvrRpm1*) in Col-0, *sgn1*, and *bik1* leaves. Data are means ± SD (n = 5). Different letters indicate significant differences (Tukey's HSD test; P < 0.05).

g, Mobility shift assay for CIF-induced BIK1 phosphorylation. Col-0 protoplasts transiently expressing BIK1-HA or SGN1-HA together with eGFP or SGN3-eGFP were treated with mock (distilled water) or the indicated flg22 and CIF peptides (1 µM) for 1 h. Protein extracts were analyzed by immunoblotting using anti-HA antibody to detect BIK1 and SGN1. Coomassie blue staining (CBB) served as a loading control. M, mock.

h, Schematic illustration of the RiD assay used to induce FLS2-BAK1 or SGN3-BAK1 complex formation and assess downstream phosphorylation of BIK1 or SGN1. PM, plasma membrane; myr, myristoylation signal; Rap, rapamycin.

i, RiD assay for SGN3-mediated BIK1 phosphorylation. *N. benthamiana* leaves transiently expressing FLS2 KD-FKBP or SGN3 KD-FKBP together with BAK1 KD-FRB and either BIK1-GFP or SGN1-GFP were treated with mock (0.1% DMSO) or rapamycin (1 µM) for 3 h. Protein extracts were analyzed by immunoblotting using anti-HA and anti-Myc antibodies to detect chimeric receptors and anti-GFP antibody to detect BIK1 or SGN1. M, mock; Rap, rapamycin.

j, Phloroglucinol staining of Col-0, SGN3^{WT}-eGFP/*sgn3*, *bik1*, and SGN3^{WT}-eGFP/*sgn3 bik1* leaves infiltrated with mock or *Pst* DC3000 (*AvrRpm1*) at 2 dpi. Boxed regions are shown at higher magnification below. Scale bars, 500 µm.

k, Quantification of lignin content in leaves as shown in (**j**). Data are means ± SD (n = 3; 3–9 leaves each). Different letters indicate significant differences (Tukey's HSD test; P < 0.05).

l, Cell death phenotypes of Col-0, SGN3^{WT}-eGFP/*sgn3*, *bik1*, and SGN3^{WT}-eGFP/*sgn3 bik1* leaves infiltrated with mock or *Pst* DC3000 (*AvrRpm1*). M, mock; R, *Pst* DC3000 (*AvrRpm1*).

m, Quantification of leaves (n = 30) with spreading cell death as shown in (**l**).

n, Bacterial growth of *Pst* DC3000 (*AvrRpm1*) in Col-0, SGN3^{WT}-eGFP/*sgn3*, *bik1*, and SGN3^{WT}-eGFP/*sgn3 bik1* leaves. Data are means ± SD (n = 5). Different letters indicate significant differences (Tukey's HSD test; P < 0.05).

o, Phloroglucinol staining of Col-0, SGN3^{WT}-eGFP/*sgn3*, *bik1*, and SGN3^{WT}-eGFP/*sgn3 bik1* seedlings treated with mock or CIF1 peptide for 3 days.

Six-week-old leaves were infiltrated with mock (10 mM $MgCl_2$) or the indicated *Pst* DC3000 strains at 1 × 10^6 CFU ml^{-1} (**f, n**) or 1 × 10^8 CFU ml^{-1} (**a**–**e, j**–**m**). Twelve-day-old seedlings were treated with mock (distilled water) or 1 µM CIF1 peptide (**o**). *hrcC*$^-$, *Pst* DC3000 *hrcC*$^-$; DC3000, *Pst* DC3000; *AvrRpm1*, *Pst* DC3000 (*AvrRpm1*); hpi, hours post-inoculation; dpi, days post-inoculation.

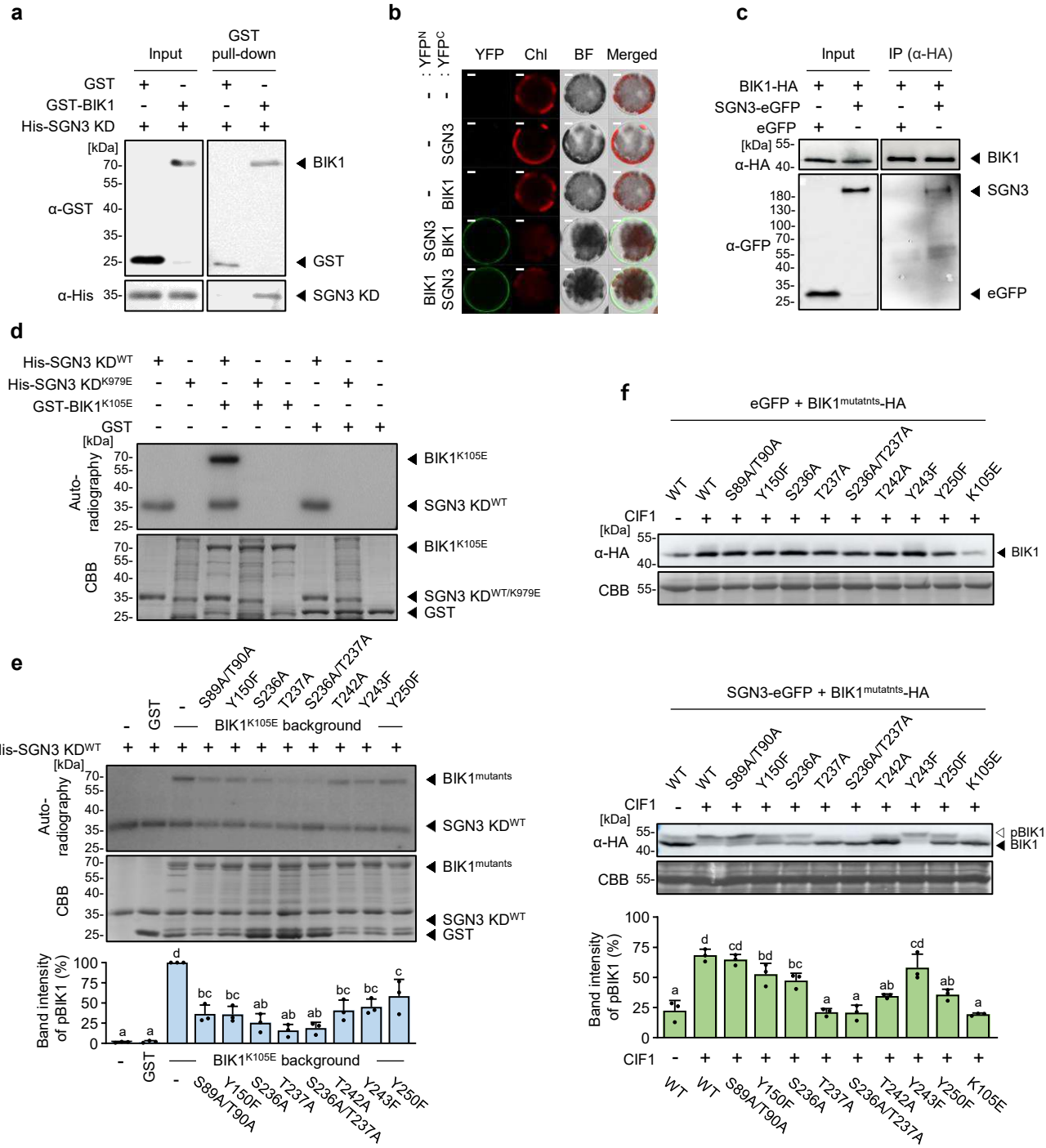

a
Input
GST pull-down
GST
GST-BIK1
His-SGN3 KD
[kDa]
α-GST
α-His
BIK1
GST
SGN3 KD
b
YFP
Chl
BF
Merged
SGN3
BIK1
c
Input
IP (α-HA)
BIK1-HA
SGN3-eGFP
eGFP
α-HA
α-GFP
BIK1
SGN3
eGFP
d
His-SGN3 KD^WT
His-SGN3 KD^K979E
GST-BIK1^K105E
GST
Auto-radiography
CBB
BIK1^K105E
SGN3 KD^WT
SGN3 KD^WT/K979E
GST
e
BIK1^K105E background
His-SGN3 KD^WT
BIK1^mutants
SGN3 KD^WT
GST
Band intensity of pBIK1 (%)
S89A/T90A
Y150F
S236A
T237A
S236A/T237A
T242A
Y243F
Y250F
f
eGFP + BIK1^mutatnts-HA
SGN3-eGFP + BIK1^mutatnts-HA
CIF1
WT
S89A/T90A
Y150F
S236A
T237A
S236A/T237A
T242A
Y243F
Y250F
K105E
α-HA
CBB
BIK1
pBIK1
Band intensity of pBIK1 (%)

Fig. 5. SGN3 interacts with and phosphorylates BIK1.
a, GST pull-down assay for *in vitro* interaction between SGN3 and BIK1. Recombinant GST or GST-BIK1 (5 μg) was incubated with His-SGN3 KD (5 μg) and pulled down using glutathione Sepharose 4B beads. Proteins were detected by immunoblotting using anti-GST and anti-His antibodies. Input shows 2% of the amount used in binding reactions.
b, BiFC assay for *in vivo* interaction between SGN3 and BIK1. YFP^N, YFP^C, and their fusions with SGN3 and BIK1 (SGN3-YFP^N, SGN3-YFP^C, BIK1-YFP^N, and BIK1-YFP^C) were co-expressed in Col-0 protoplasts for 20–24 h. Reconstituted YFP fluorescence was visualized under a confocal microscope. Chl, chlorophyll; BF, bright field. Scale bars, 10 μm.
c, Co-immunoprecipitation assay for *in vivo* interaction between SGN3 and BIK1. Protein extracts from Col-0 protoplasts co-expressing SGN3-eGFP and BIK1-HA were immunoprecipitated with anti-HA antibody and analyzed by immunoblotting using anti-HA and anti-GFP antibodies. Input shows 2% of the amount used in binding reactions. IP, immunoprecipitation.
d, *In vitro* kinase assay for SGN3-mediated BIK1 phosphorylation. Recombinant His-SGN3 KD^{WT} or His-SGN3 KD^{K979E} (1 μg) was incubated with GST or GST-$BIK1^{K105E}$ (1 μg). The kinase reaction mixtures were resolved by SDS-PAGE and radioactive signals were detected by autoradiography. Protein loading was shown by Coomassie blue staining (CBB).
e, *In vitro* kinase assay to identify BIK1 phosphosites targeted by SGN3. Residues additionally mutated in the $BIK1^{K105E}$ background are indicated above each lane. Recombinant His-SGN3 KD^{WT} (1 μg) was incubated with GST or GST-$BIK1^{K105E}$ phosphosite mutants (1 μg). The kinase reaction mixtures were resolved by SDS-PAGE and radioactive signals were detected by autoradiography. Protein loading was shown by Coomassie blue staining (CBB). The graph shows phosphorylation levels of GST-$BIK1^{K105E}$ phosphosite mutants quantified relative to GST-$BIK1^{K105E}$. Data are means ± SD (n = 3). Different letters indicate significant differences (Tukey's HSD test; $P < 0.05$).
f, Mobility shift assay to identify SGN3-dependent BIK1 autophosphorylation sites. Residues mutated in BIK1 are indicated above each lane. Col-0 protoplasts transiently expressing BIK1-HA or BIK1 phosphosite mutants-HA together with eGFP or SGN3-eGFP were treated with mock (distilled water) or 1 μM CIF1 peptide for 1 h. Protein extracts were analyzed by immunoblotting using anti-HA antibody. Coomassie blue staining (CBB) served as a loading control. The graph shows CIF1-induced BIK1 phosphorylation quantified relative to total BIK1 protein levels. Data are means ± SD (n = 3). Different letters indicate significant differences (Tukey's HSD test; $P < 0.05$).

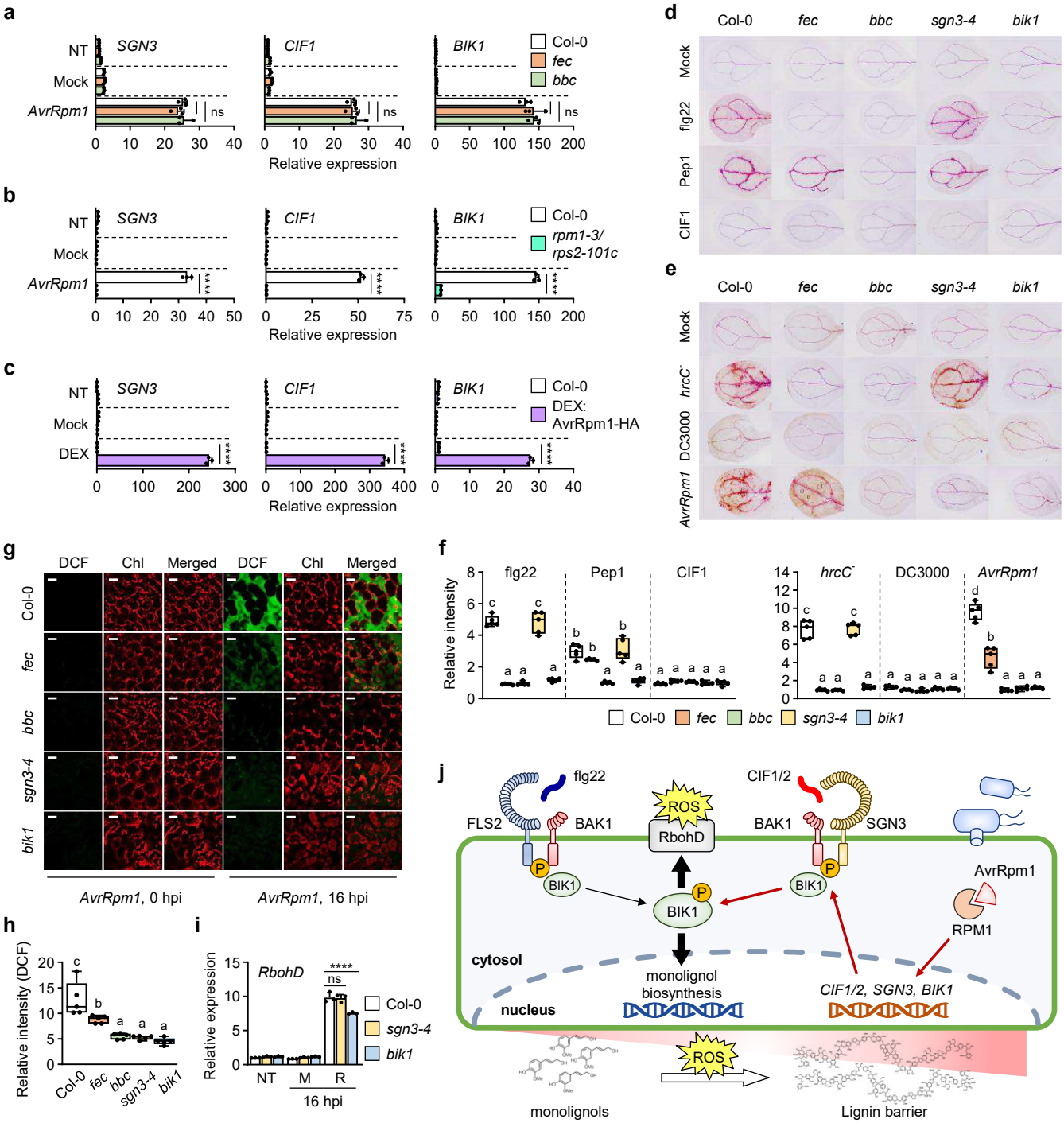

a
NT
Mock
AvrRpm1
SGN3
CIF1
BIK1
Col-0
fec
bbc
ns
Relative expression
b
rpm1-3/
rps2-101c
****
c
DEX
DEX:
AvrRpm1-HA
d
Col-0
fec
bbc
sgn3-4
bik1
Mock
flg22
Pep1
CIF1
e
hrcC-
DC3000
AvrRpm1
f
Relative intensity
flg22
Pep1
CIF1
hrcC-
DC3000
AvrRpm1
g
DCF
Chl
Merged
AvrRpm1, 0 hpi
AvrRpm1, 16 hpi
h
Relative intensity (DCF)
i
RbohD
Relative expression
NT
M
R
16 hpi
j
flg22
FLS2
BAK1
ROS
RbohD
CIF1/2
SGN3
BIK1
P
AvrRpm1
RPM1
cytosol
nucleus
monolignol
biosynthesis
CIF1/2, SGN3, BIK1
monolignols
Lignin barrier

Fig. 6. NLR-activated SGN3 signaling co-opts PTI components to coordinate lignification during ETI.
a-c, Expression of *SGN3*, *CIF1*, and *BIK1* in Col-0, *fec*, and *bbc* (**a**), *rpm1-3 rps2-101c* (**b**), and Dex:AvrRpm1 (**c**) leaves infiltrated with mock or *Pst* DC3000 (*AvrRpm1*) (**a, b**), and with mock or dexamethasone (DEX) (**c**) at 16 hpi. Data are means ± SD (n = 3). Asterisks indicate significant differences relative to the no-treatment control (NT) (t test; ****P < 0.0001).
d, Phloroglucinol staining of Col-0, *fec*, *bbc*, *sgn3*, and *bik1* seedlings treated with mock or flg22, Pep1, and CIF1 peptides for 3 days.
e, Phloroglucinol staining of Col-0, *fec*, *bbc*, *sgn3*, and *bik1* seedlings flood-inoculated with mock or the indicated *Pst* DC3000 strains at 3 dpi.
f, Quantification of phloroglucinol-stained lignin in leaves as shown in (**d**, **e**). Data are means ± SD ($n \geq 3$). Different letters indicate significant differences (Tukey's HSD test; $P < 0.05$).
g, Representative microscopic images of ROS accumulation detected by DCF fluorescence in Col-0, *fec*, *bbc*, *sgn3*, and *bik1* leaves infiltrated with mock or *Pst* DC3000 (*AvrRpm1*) at 16 hpi. Chl, chlorophyll. Scale bars, 50 μm.
h, Quantification of DCF fluorescence intensity at 16 hpi as shown in (**g**). Data are means ± SD ($n \geq 3$). Different letters indicate significant differences (Tukey's HSD test; $P < 0.05$).
i, Expression of *RbohD* in Col-0, *sgn3*, and *bik1* leaves infiltrated with mock or *Pst* DC3000 (*AvrRpm1*) at 16 hpi. Data are means ± SD (n = 3). Asterisks indicate significant differences relative to the no-treatment control (NT) (t test; ****P < 0.0001). M, mock; R, *Pst* DC3000 (*AvrRpm1*).
j, A model for the role of CIFs-SGN3-BIK1 signaling during ETI. Upon effector recognition, NLR signaling rapidly upregulates CIF1/2 peptides, their receptor SGN3, and BIK1 at the transcriptional level, enabling prompt assembly and activation of the SGN3 signaling module. Activated SGN3 engages BIK1 and acts in concert with PRR pathways to enhance BIK1 phosphorylation and activation. This convergent signaling promotes monolignol biosynthesis and a robust ROS burst, leading to localized lignin deposition. The resulting lignin-based physical barrier restricts pathogen spread and spatially confines hypersensitive cell death, thereby reinforcing disease resistance during ETI.
Six-week-old leaves were infiltrated with mock (10 mM $MgCl_2$) or *Pst* DC3000 (*AvrRpm1*) at 1×10^8 CFU ml^{-1} (**a, b, g**–**i**) and with mock (0.1% DMSO) or 10 μM DEX (**c**). Twelve-day-old seedlings were treated with mock (distilled water) or 1 μM peptides (**d, f**), and with mock (10 mM $MgCl_2$) or the indicated *Pst* DC3000 strains at 1×10^8 CFU ml^{-1} (**e, f**). *hrcC*$^-$, *Pst* DC3000 *hrcC*$^-$; DC3000, *Pst* DC3000; *AvrRpm1*, *Pst* DC3000 (*AvrRpm1*); ns, not significant; hpi, hours post-inoculation.

Supplementary Files

This is a list of supplementary files associated with this preprint. Click to download.

- NaturePlantsSupplTable1.xlsx
- NaturePlantsSupplFigures.pdf
- NaturePlantsReportingSummary.pdf